

# Breaking and non-breaking solitary wave impact pressures on a cylinder over a 3-D bathymetry

Charlie Bisgard

A project report submitted in partial fulfillment of the requirements for the  
degree of

Master of Science

Oregon State University

2005

Program Authorized to offer Degree:  
Department of Civil and Environmental Engineering and Construction  
Management

Report Documentation Page				Form Approved OMB No. 0704-0188	
Public reporting burden for the collection of information is estimated to average 1 hour per response, including the time for reviewing instructions, searching existing data sources, gathering and maintaining the data needed, and completing and reviewing the collection of information. Send comments regarding this burden estimate or any other aspect of this collection of information, including suggestions for reducing this burden, to Washington Headquarters Services, Directorate for Information Operations and Reports, 1215 Jefferson Davis Highway, Suite 1204, Arlington VA 22202-4302. Respondents should be aware that notwithstanding any other provision of law, no person shall be subject to a penalty for failing to comply with a collection of information if it does not display a currently valid OMB control number.					
1. REPORT DATE <b>01 MAR 2005</b>		2. REPORT TYPE <b>N/A</b>		3. DATES COVERED <b>-</b>	
4. TITLE AND SUBTITLE <b>Breaking and non-breaking solitary wave impact pressures on a cylinder over a 3-D bathymetry</b>				5a. CONTRACT NUMBER	
				5b. GRANT NUMBER	
				5c. PROGRAM ELEMENT NUMBER	
6. AUTHOR(S)				5d. PROJECT NUMBER	
				5e. TASK NUMBER	
				5f. WORK UNIT NUMBER	
7. PERFORMING ORGANIZATION NAME(S) AND ADDRESS(ES) <b>Oregon State University</b>				8. PERFORMING ORGANIZATION REPORT NUMBER	
9. SPONSORING/MONITORING AGENCY NAME(S) AND ADDRESS(ES)				10. SPONSOR/MONITOR'S ACRONYM(S)	
				11. SPONSOR/MONITOR'S REPORT NUMBER(S)	
12. DISTRIBUTION/AVAILABILITY STATEMENT <b>Approved for public release, distribution unlimited</b>					
13. SUPPLEMENTARY NOTES <b>The original document contains color images.</b>					
14. ABSTRACT					
15. SUBJECT TERMS					
16. SECURITY CLASSIFICATION OF:			17. LIMITATION OF ABSTRACT <b>UU</b>	18. NUMBER OF PAGES <b>95</b>	19a. NAME OF RESPONSIBLE PERSON
a. REPORT <b>unclassified</b>	b. ABSTRACT <b>unclassified</b>	c. THIS PAGE <b>unclassified</b>			

## Table of Contents

Table of Contents.....	ii
List of Figures.....	iv
List of Tables.....	vi
Chapter 1.....	1
INTRODUCTION.....	1
Chapter 2.....	5
LITERATURE REVIEW.....	5
2.1    Setting up the experiment.....	5
2.2    Impact pressures from a breaking wave.....	7
2.3    Modeling the force from a broken wave.....	8
2.4    Modeling the force from a unbroken wave.....	10
2.4.1    The Morison equation.....	10
Chapter 3.....	13
SET UP.....	13
3.1    Tsunami wave basin.....	13
3.2    Existing model and bathymetry.....	16
3.3    Modifications to existing model.....	18
Chapter 4.....	19
INSTRUMENTATION AND DATA ACQUISITION.....	19
4.1    INSTRUMENTS.....	19
4.1.1    ADV's.....	19
4.1.2    Wave gauges.....	22
4.1.3    Pressure sensors.....	22
4.2    Method of deployment.....	24
4.3    Wait time between runs.....	26
4.4    Repeatability level of velocity measurements.....	27
4.5    Testing plan.....	28
4.5.1    Cases.....	28
4.5.2    Wave gauges and ADV's.....	32
Chapter 5.....	46
RESULTS.....	46
5.1    ADV's.....	46
5.2    Wave gauges.....	48
5.3    Pressure sensors.....	50
5.3.1    Varying wave height.....	51
5.3.2    Varying y-location (crosstank).....	54
5.3.2    Varying cylinder orientation.....	58
Chapter 6.....	66
ANALYSIS.....	66
6.1    Conversion of measured pressures to force.....	66
6.1.1    Impact force on a wedge of the cylinder.....	66
6.1.2    Resultant impact force on the cylinder.....	74

6.1.3	Resultant direction of the impact force .....	75
6.2	Determining the period (T) of cases 1 and 2.....	76
6.2.1	Period from estimated method .....	76
6.2.2	Period from theoretical method .....	76
6.3	Morison equation approximation for case 2 .....	78
6.3.1	Results from the Morison equation applied to case 2 .....	78
6.3	Cross approximation for case 1.....	80
Chapter 7	.....	82
CONCLUSION	.....	82
7.1	Estimation of broken wave force .....	82
7.2	Estimation of unbroken wave force .....	82
7.3	Future works and recommendations .....	83
BIBLIOGRAPHY	.....	84
APPENDIX	.....	86
Appendix 1	.....	86

## List of Figures

Figure 1, CERC layout.....	6
Figure 2, Sketch showing the wedge angle of the incoming bore approaching the wall, Cross (1967).....	9
Figure 3, Sketch of Wave forces on a cylinder, SPM Vol II .....	11
Figure 4, Sketch of the TWB waveboard from MTS engineering drawings .....	14
Figure 5, Sketch of an individual paddle from the TWB waveboard from MTS engineering drawings .....	14
Figure 6, Picture of solitary wave produced by the TWB wavemaker .....	15
Figure 7, TWB layout .....	15
Figure 8, Plot of survey data .....	17
Figure 9, Image produced from the LIDAR scan .....	17
Figure 10a, Picture of extended wall      Figure 10b, Picture of wedge.....	18
Figure 11, Spreading out the mixed seeding material.....	21
Figure 12, Mixing the dry seeding material with fresh basin water .....	21
Figure 13, Pressure sensor calibration .....	23
Figure 14, Picture of frame on the bridge and frame .....	24
Figure 15, Picture of 4 pairs of wave gauges and ADVs mounted on the frame.....	25
Figure 16, Picture of flush mounted pressure sensors, and 50lb top weight .....	26
Figure 17, Plot of standard deviation taken at every minute vs. time. Taken from an ADV which was located in the center of the TWB at an offshore location, for the wave from case 1.....	27
Figure 18, Repeatability plots for the ADV .....	28
Figure 19, Solitary wave control signal showing the displacement of the waveboard.....	31
Figure 20, Incident water surface elevation at the wave board.....	32
Figure 21, Testing locations for WGs and ADVs, for offshore depth of 55cm, Cases 1 and 2.....	33
Figure 22, Testing locations for WGs and ADVs, for offshore depth of 44cm, Cases 3 and 4.....	34
Figure 23, Plots of raw data from WGs and ADVs for case 1.....	36
Figure 24, Plots of raw data from WGs and ADVs for case 2.....	36
Figure 25, Plots of raw data from WGs and ADVs for case 3.....	37
Figure 26, Plots of raw data from WGs and ADVs for case 4.....	37
Figure 27, Comparison plot of the horizontal velocities produced by each case, measured at the same offshore location. ....	38
Figure 28, Pressure Testing Grid .....	39
Figure 29, Pressure time series for case 1 .....	42
Figure 30, Pressure time series for case 2.....	42
Figure 31, Pressure time series for case 3.....	43
Figure 32, Pressure time series for case 4.....	43
Figure 33, Magnification of pressure spike for case 1 .....	44
Figure 34, Magnification of pressure spike for case 3.....	44
Figure 35, Vector Plots of Maximum Velocity .....	47

Figure 36, MATLAB Plot Showing 3 Wave Gauge Points along the Centerline of the Harbor .....	48
Figure 37, Measured Wave Heights for Cases 1 and 2 .....	49
Figure 38, Locations used for pressure-cylinder tests .....	50
Figure 39, Picture of dry harbor with cylinder in the harbor location of $x=18$ m, $y=16$ m. ....	51
Figure 40, Pressure Time Histories for Increasing H at Pressure Sensor 2 .....	52
Figure 41, Pressure Time Histories for Increasing H at Pressure Sensor 3 .....	52
Figure 42, Pressure time histories for increasing cross-shore distance at pressure sensor 2 .....	55
Figure 43, Pressure time histories for increasing cross-shore distance at pressure sensor 3 .....	56
Figure 44, Pressure time histories for increasing cross-shore distance at pressure sensor 2 .....	57
Figure 45, Pressure time Histories for increasing cross-shore distance at pressure sensor 3 .....	57
Figure 46, Pressure Time histories for orientations 1-151 degrees, at pressure sensor 2 ..	59
Figure 47, Pressure time Histories for orientations 181-331 degrees, at pressure sensor 2 .....	60
Figure 48, Pressure distribution around the cylinder, case1 .....	61
Figure 49, Pressure time histories for orientations 7-157 degrees, at pressure sensor 2 ..	62
Figure 50, Pressure time histories for orientations 187-337 degrees, at pressure sensor 2 .....	63
Figure 51, Pressure distribution around the cylinder, case2 .....	64
Figure 52, Pressure distribution on a cylinder, in steady flow (Schlichting, 1979).....	64
Figure 53, Diagram of case 2 impacting the cylinder .....	68
Figure 54, Plot of pressures along the vertical cylinder face for case 2 .....	69
Figure 55, Diagram of case 1 impacting the cylinder .....	70
Figure 56, Plot of pressures along cylinder face for case 1 .....	71
Figure 57, Distribution of wave pressure on an upright section of a vertical breakwater.	72
Figure 58, Force on each wedge orientation, case 1 .....	73
Figure 59, Force on each wedge orientation, case 2 .....	74
Figure 60, Diagram of long and crosstank force components, and resultant force .....	75
Figure 61, Plots of cases 1 and 2.....	76
Figure 63, Plot of $C_f$ versus $\theta$ .....	80
Figure 64, Cross method for case 1 .....	81
Figure 65, Group Photo of Project Team.....	86

## **List of Tables**

Table 1, Comparison of experimental setups.....	6
Table 2, Case Types and Descriptive Parameters .....	28
Table 3, Pressure Impact Tests Performed, and Cases Run.....	40
Table 4, Period values for waves cases 1 and 2, using measured and theoretical methods .....	77
Table 5, Guide for evaluating wave load calculation procedures (Randal, 01).....	78
Table 6, Case 2, values from measured and theoretical periods (T).....	79
Table 7, Comparison of maximum force on the cylinder, case 2 .....	80

## List of Symbols

### Roman Letters

$c$	Wave celerity
$C^*$	See equation 4.2
$C_d$	Coefficient of drag
$C_f$	Force Coefficient
$C_m$	Coefficient of inertia
$d$	water depth
$D$	Diameter
$Disp$	Displacement of waveboard
$erf$	Error function
$F$	Total force
$f_d$	Drag force per unit length
$F_f$	Force coefficient
$f_m$	Inertial force per unit length
$f_i$	Total force per unit length
$h$	Bore height
$H$	Wave height
$H_o$	Offshore wave height
$Ke$	Keulegan-Carpenter number
$h_{ws}$	Height of still water level
$h_2$	Height of pressure sensor 2
$I$	Current
$k$	Wave number
$L$	Wavelength
$P$	Pressure
$P_{max}$	Maximum pressure
$p_b$	Pressure at the bottom of the cylinder
$p_{ws}$	Pressure at the free water surface
$p_2$	Pressure at pressure sensor 2
$R$	Resistance
$Re$	Reynolds number
$t$	Time
$t^*$	Time taken during the forward displacement of the wavemaker
$T$	Wave period
$u$	Horizontal water particle velocity in x-direction
$Um$	Peak water particle velocity
$V$	Voltage
$w$	Width of cylinder slice or wedge
$x$	Long-shore location
$X_o$	Instantaneous wave board position
$y$	Cross-shore location
$z$	Vertical location

### Greek Letters

$\kappa$	See equation 4.3
----------	------------------



$\sigma$	Angular frequency
$\rho$	Water density
$\gamma$	Specific weight
$\eta$	Free surface elevation
$\nu$	Kinematic viscosity

## Chapter 1

### INTRODUCTION

A tsunami is a wave or a series of waves principally generated by undersea earthquakes of magnitude greater than 6.5 on the Richter scale. These long period waves can also be created by other natural disturbances such as landslides, volcanic eruptions, and explosions near the sea surface. The word *tsunami* is used in place of tidal wave to remove any confusion with the astronomical tides. The word tsunami comes from the Japanese words “tsu” (harbor) and “nami” (wave) and is used to describe the large waves that are seismically produced (SPM, Vol 1).

Tsunamis in general are the product of earthquakes that extend at least partially under the sea. These earthquakes or other undersea disruptions cause sudden vertical changes in the seafloor, which in turn cause a large volume of water to be displaced from its equilibrium position to a new position of rise or depression. This change in equilibrium then moves outwards from the source of origin in the form of a tsunami. Due to the way that tsunamis are generated, the energy of the tsunami waves are evenly distributed throughout the entire water column. This differentiates tsunamis from the common wind generated waves, in that wind waves in deepwater have most of their energy held in the

region of the water column near to the surface. Tsunamis are extremely long waves with long periods that can range from five minutes to several hours. Due to their very long wavelengths, tsunamis travel at the shallow water wave celerity which is equal to the square root of the gravitational acceleration times the water depth. The speed of a tsunami in the open ocean can reach in excess of 500 miles per hour. Tsunamis are also characterized by low wave height when moving through oceanic depths and are often hard to recognize when seen out in the deep ocean (Wikipedia, 2005).

As tsunamis approach the coastal region, they are affected by the rapid decrease in water depth. As they approach shore, tsunamis are also affected by the processes of wave refraction, shoaling, and bay or harbor resonance. Due to the significant period and wavelength of tsunamis, they are often seen as a rapidly rising water level, or a broken wave bore approaching the shoreline (Wikipedia, 2005).

The loss of both life and property due to tsunamis has been immense. The December 2004 Indian Ocean earthquake, tsunami, and the resultant floods caused approximately 283,000 fatalities, 14,100 people to go missing, and thousands others to be displaced. This tsunami destroyed the shores of Indonesia, Sri Lanka, South India, Thailand, and other surrounding countries with wave heights up to 100 ft. Damage to coastal structures was seen to be from both the impact of floating debris, and the force of the flow itself. Prior to 2004, the deadliest tsunami was in 1782, when 40,000 people were killed in the South China Sea (Wikipedia, 2005).

Despite advances in both hydrodynamics and seismology, the processes of three dimensional tsunami run-up is still an area not fully understood. Run-up or tsunami

inundation is the main focus of coastal engineers because it affects the coastal population the most (Briggs, 1994).

The goal of this project was to create a benchmark set of wave data collected over a three dimensional, complex bathymetry for numerical models of tsunami inundation. This set of data will be placed online as part of the shared-use concept of the National Science Foundation's Network for Earthquake Engineering Simulation (NEES) program. Once uploaded, these data will increase the limited laboratory and field data that are essential for verifying or refuting numerical models. Numerical models enable and increase the ability to provide awareness, preparation, and response to potential tsunami disasters. This project focused on collecting laboratory data that explored tsunami inundation and impact forces. The analysis portion of this project focuses on physical modeling of a rigid, free-standing cylinder subjected to the passing of a tsunami modeled by both a turbulent bore and a non-breaking wave. Measurements were made of surface levels and velocity of the passing water as well as the pressures acting on the cylinder. The goal is to observe how well theories can predict the measured wave forces encountered in testing.

In 2005, there were 5 other reports which used the same or similar 3D bathymetry as was used for this project. These reports include:

- Design and Implementation of a Physical Model for Keystone Harbor, Washington, (Brady, 2005)
- Keystone Phase II: Alteration of the Harbor and Relocation of the Jetty (Bisgard, Grier, Ichikawa, 2005, unpublished report)

- 3D Physical Model of Tsunami Inundation over a Complex Bathymetry (Lynch, 2005, unpublished REU report)
- Laboratory observations of Tsunami run-up velocity on a complex 3d bathymetry using PIV (Ichikawa, 2005)

Of these reports, the Masters Thesis by Ichikawa (2005) and REU report by Lynch (2005) used exactly the same bathymetry and wave conditions and can be considered companion reports. Data from Ichikawa (2005) and Lynch (2005) are included in the online data set.

## Chapter 2

### LITERATURE REVIEW

#### **2.1 Setting up the experiment**

This project involved the collecting of free surface, velocity, and pressure from solitary waves over a large three dimensional basin. Briggs (1994) provided a good example of how to set-up the instrumentation for this experiment. Through an experiment of running solitary waves at a circular island, Briggs was able to collect characteristic wave data in a large three dimensional (3D) basin. The experiments were performed at the Coastal Engineering Research Center (CERC) in Vicksburg, Mississippi and used a 30 m wide by 25 m long wave basin, which is comparable to the 48.8 m long by 26.5 m wave basin used for our experiment. Figure 1 shows a schematic of the basin used at CERC.

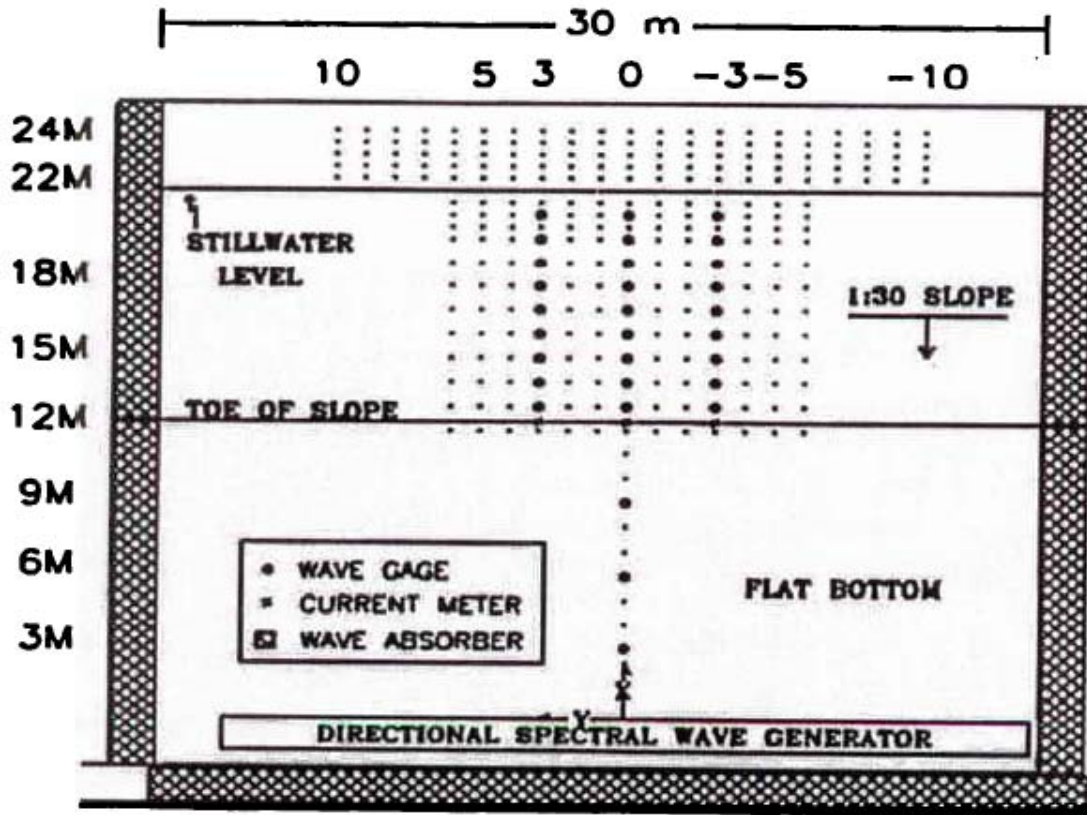


**Figure 1, CERC layout**

The Briggs experiment still water depth of 32 cm was also similar to still water depths of 44 cm and 55 cm used in our experiment. In addition the solitary wave heights used by the Briggs experiment were in the range of 10 cm to 50 cm, which was similar to the range of 5 cm to 25 cm wave heights that we used. A comparison of the Briggs experiment and the Tsunami Inundation experiment can be seen in Table 1.

**Table 1, Comparison of experimental setups**

	offshore depth (cm)	width (m)	length (m)	maximum $H_o$ (cm)	type -	bathymetry -
Briggs (1994)	32	30	25	20	solitary	1:30 plane beach
Tsunami Inundation (2005)	44 and 55	26.5	48.8	25	solitary	complex 3D

The maximum wave height used by Briggs at CERC was only 20 cm due to the stroke limitations of their wavemaker. The TWB wavemaker was able to produce larger solitary

waves, which enabled wave heights ranging from 5 to 25 cm to be tested. The complex 3D bathymetry used in the Tsunami Inundation experiment provided a more realistic and complex bathymetry for scientists to test their models on.

The Briggs experiment also provided an example of what type of longshore spacing we could use for our water surface and water velocity measuring instruments. In the Briggs experiment the instruments were spaced every three meters in the longshore direction.

Similarly, our instruments had long shore spacing of every two meters in the along shore direction.

## **2.2 Impact pressures from a breaking wave**

Often the pressure time history of a wave impacting on a cylinder is difficult to analyze, especially if the wave is breaking at the point where the cylinder is located. For a wave breaking on a cylinder the pressure time history will show a large spike at initial impact, followed by a reduced more gradual history of pressure decrease. Wienke and Oumeraci (2004) divide this impact pressure into two components. The initial pressure spike is called the dynamic component, and is caused by the very short effect of the wave face slamming into the cylinder profile. The remaining pressure time history is called the quasi-static component and can be treated as the result of a non-breaking wave impacting the cylinder. Equation 2.1 shows the force equation that accounts for the quasi-static and dynamic components.

$$f_t = f_d + f_m + f_i \quad (2.1)$$

The terms  $f_d$  and  $f_m$  are the drag and inertial force per unit length, they make up the static component of the breaking wave force. The terms  $f_i$  and  $f_t$  are the impact and total force per unit length



### 2.3 Modeling the force from a broken wave

In modeling the force from a broken wave, it was first necessary to understand what form the wave takes after it has broken but still progressing toward shore. The broken wave which enters the harbor appears as a bore tumbling through the harbor. Acosta (1971) describes the broken wave moving towards shore as “the movement of a high-water front into an undisturbed region of lower water level we shall call a positive surge...the solution for this surge can be obtained from that for the hydraulic jump by single superposition” (Acosta, 1971). Often the progressing bore is compared to a hydraulic jump, except that the bore is moving and a hydraulic jump is static.

Next in analyzing the progressing bore, it is necessary to determine properties or characteristics of the bore that are representative of the force the bore will deliver onto a structure. Obviously the water velocity and water surface as a function of time are important quantitative properties. In addition, Cumberpatch (1960) used a property of the bore called the wedge angle as another way to characterize the bore. This wedge angle can be described as the angle that the bore makes with the bottom. A steep bore will have a high wedge angle, and a shallow flat bore will have a low wedge angle.

Cumberpatch defined a force coefficient which relates the force on the wall to the momentum flux which would occur at the wall location if the wall were not present. This force coefficient ( $C_f$ ) seen in equation 2.2, is multiplied by the water density ( $\rho$ ), the width of the wall ( $b$ ), the bore height ( $h$ ), and the celerity ( $c$ ) squared.

$$F = C_f \rho b h c^2 \quad (2.2)$$

Cross (1967) added to the concepts of Cumberbatch by adding gravitational forces to the equation for force. The Cross equation shown in equation 2.3 is an approximation to estimate the impact force on a wall from a progressing surge.

$$F = \frac{1}{2} \gamma b h^2 + C_f \rho b h u^2 \quad (2.3)$$

The first group of terms on the right hand side of the equation is the gravitational force. The second term on the right hand side of the equation is the force on the wall from the momentum flux. The term  $F$  refers to the force delivered on the wall from the incoming bore. The terms  $\gamma$ ,  $\rho$ ,  $h$ ,  $b$ , are the specific weight, the water density, the water level at the wall location, and the width of the wall. The  $C_f$  term refers to the force coefficient which is a function of only the incident wedge angle. The wedge angle is shown in Figure 2, where the symbol  $\theta$  is used for the wedge angle.

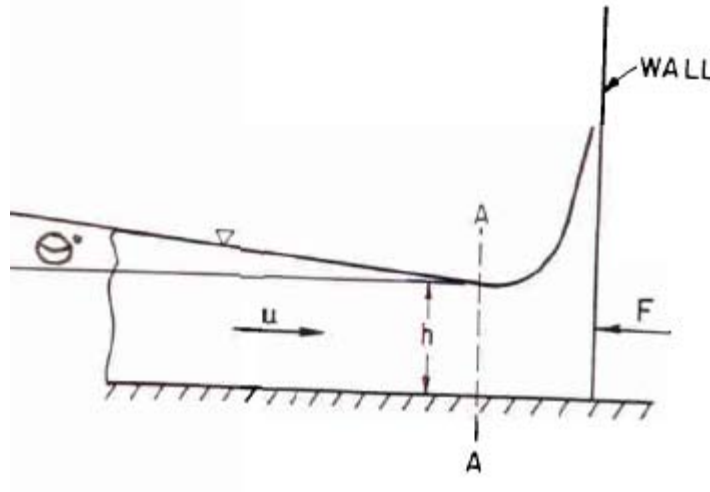


Figure 2, Sketch showing the wedge angle of the incoming bore approaching the wall, Cross (1967)

## **2.4 Modeling the force from a unbroken wave**

Randall (1997) provides guidelines for when and how to apply the Morison equation to a wave cylinder interaction. First, it is suggested that the ratio of diameter ( $D$ ) to wave length ( $L$ ) be checked to see if it is less than 0.2. If this ratio is higher than 0.2, then the Morison equation should not be used for computing wave forces, and diffraction theory should be used instead. If the ratio is less than 0.2, the wave is non-breaking, and the object is a cylinder, then the Morison equation can be used. Like the Cumberpatch and Cross methods, the underlying assumption for the Morison equation is that the wave properties are unaffected by the presence of the structure. With this known and due to limits in the availability of testing equipment, the water height and water particle velocity were tested in the absence of the cylinder.

### **2.4.1 The Morison equation**

The Morison equation is used to predict forces on a pile, or cylindrical structure, due to the wave associated flow field. Due to the complexity of wave induced flows, the equation relies on empirical coefficients to augment the theoretical formulations of the problem. The Morison equation is specifically used to determine the non-breaking forces of monochromatic waves on a cylinder. The Morison equation will be used here to see how well it can model the wave forces of case 2, which is a non-breaking wave, but is not a monochromatic wave. The variables that are important in determining the forces on cylindrical objects subjected to waves are shown in Figure 3.

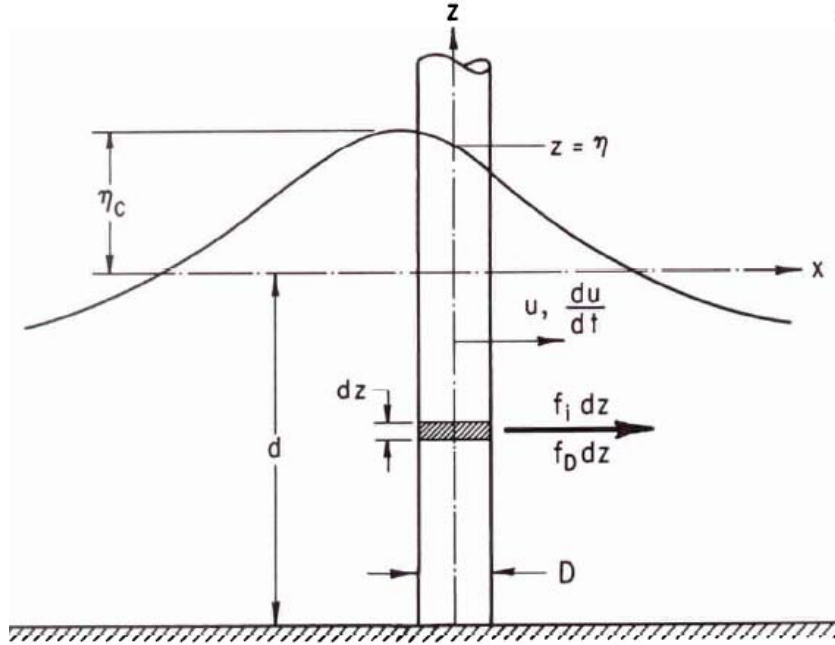


Figure 3, Sketch of Wave forces on a cylinder, SPM Vol II

In 1950 Morison published his theory that suggested that the horizontal force per unit length of a vertical cylindrical pile may be expressed by equation 2.4.

$$f_t = f_d + f_m \quad (2.4)$$

Equation 2.3 shows that the total force per unit length is equal to the inertial force per unit length plus the drag force per unit length. The term  $f_m$  is obtained from an analysis of the force on a body in an accelerated flow of an ideal non-viscous fluid. The term  $f_d$  is the drag force exerted on a cylinder in a steady flow of a real viscous fluid. Equation 2.4 can be expressed using more terms by equation 2.5.

$$f_t = C_m \rho \pi \frac{D^2}{4} \frac{du}{dt} + \frac{1}{2} C_d \rho D u^2 \quad (2.5)$$

The first part of equation 2.4 is the inertial component, and the second part is the drag component. The inertial and drag coefficients,  $C_i$  and  $C_d$ , are both empirically derived coefficients that are selected based upon the Reynolds Number ( $Re$ ) and Keulegan-Carpenter numbers ( $Ke$ ). The term  $\rho$  refers to the density of the fluid that is interacting

with the cylinder. The term  $\frac{\pi D^2}{4}$  is the cross sectional area of the cylinder. The term  $du/dt$  is the change in horizontal water particle velocity over time, or simply referred to as the acceleration of the water. The far right side of equation 6 is the drag force component. The drag force is proportional to the square of the horizontal water particle velocity ( $u$ ), and acts in the direction of  $u$  (SPM, Vol II).

## Chapter 3

### SET UP

#### **3.1 Tsunami wave basin**

All experimentation took place in the tsunami wave basin (TWB), which is located at the O.H. Hinsdale Wave Research Laboratory facility at Oregon State University. The TWB is 48.8 m long by 26.5 m by 2.1 m depth. The TWB is equipped with a piston type, electric motor driven wavemaker that has twenty nine 2 m high wave boards. This wavemaker can produce a large stroke, up to 2.1 m, and the directional wavemaker is setup with active wave absorption. This programmable wavemaker was manufactured by MTS Systems Corporation and installed in 2003. Figure 4 and Figure 5 show the wavemaker paddle, and the overall wave board. Figure 6 shows the basin soon after a solitary wave was produced by the wavemaker. Figure 7 is a schematic of the TWB.

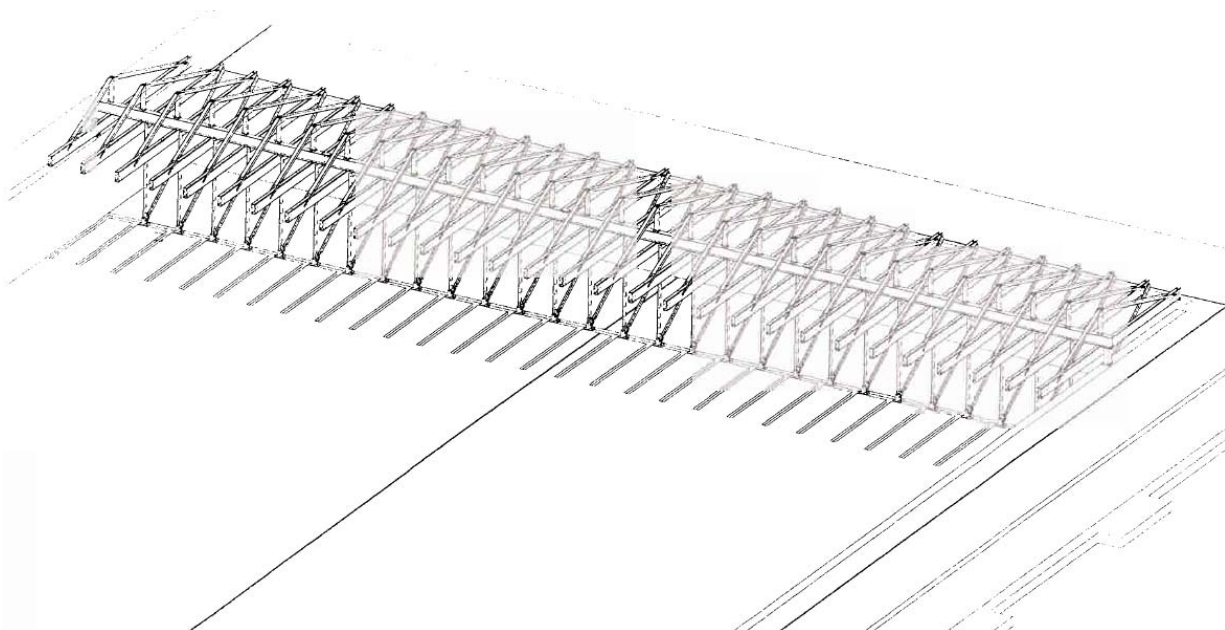


**Figure 4, Sketch of the TWB waveboard from MTS engineering drawings**

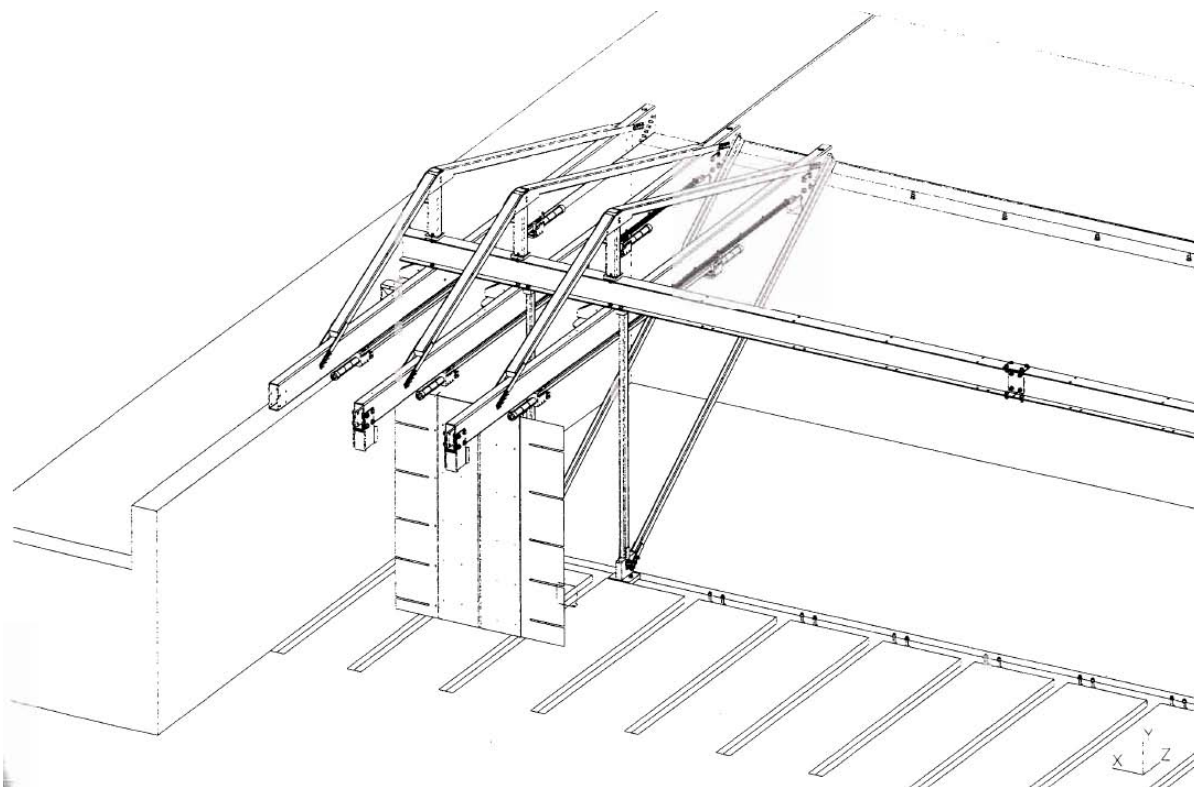


**Figure 5, Sketch of an individual paddle from the TWB waveboard from MTS engineering drawings**



**Figure 6, Picture of solitary wave produced by the TWB wavemaker**

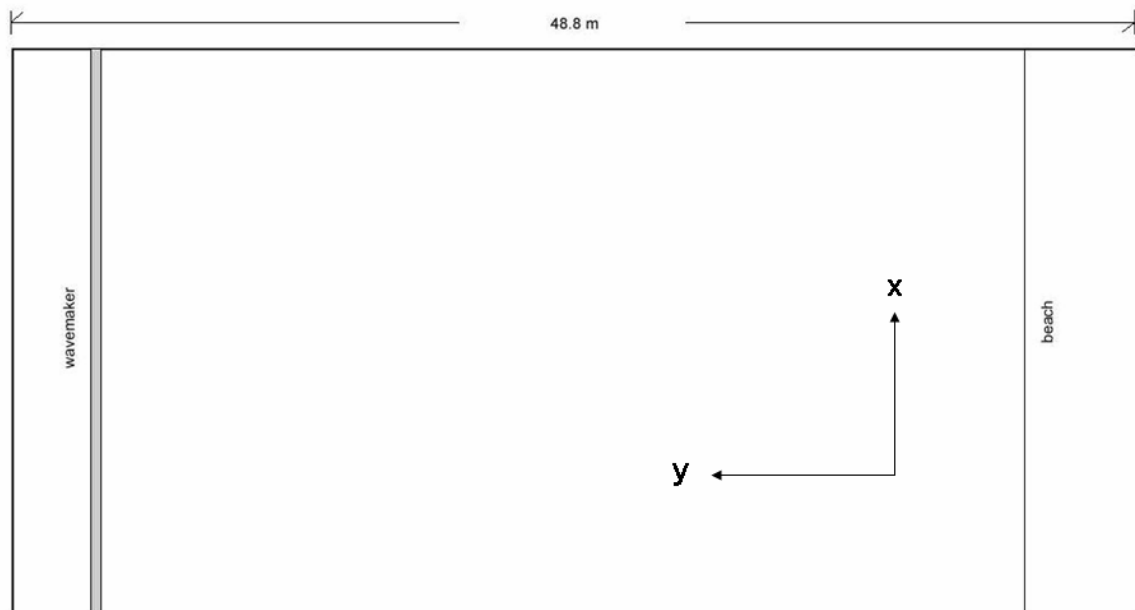


**Figure 7, TWB layout**



### **3.2 Existing model and bathymetry**

The model that provided the irregular, 3D bathymetry for our experiment was constructed as part of an earlier experiment performed in the TWB. This earlier experiment was a fixed bed, 1:40 scale model of Keystone harbor on Whidbey Island in Puget Sound. The bathymetry, seen in Figure 8, produced from the Keystone experiment was good to study because it provided realistic features of a coastal area. The model provided a coastline section that was both steep and shallow, and also provided a large harbor area. The bathymetry and the entire TWB had a LIDAR survey performed, which produced a three dimensional grid with over one million data points seen in Figure 9.

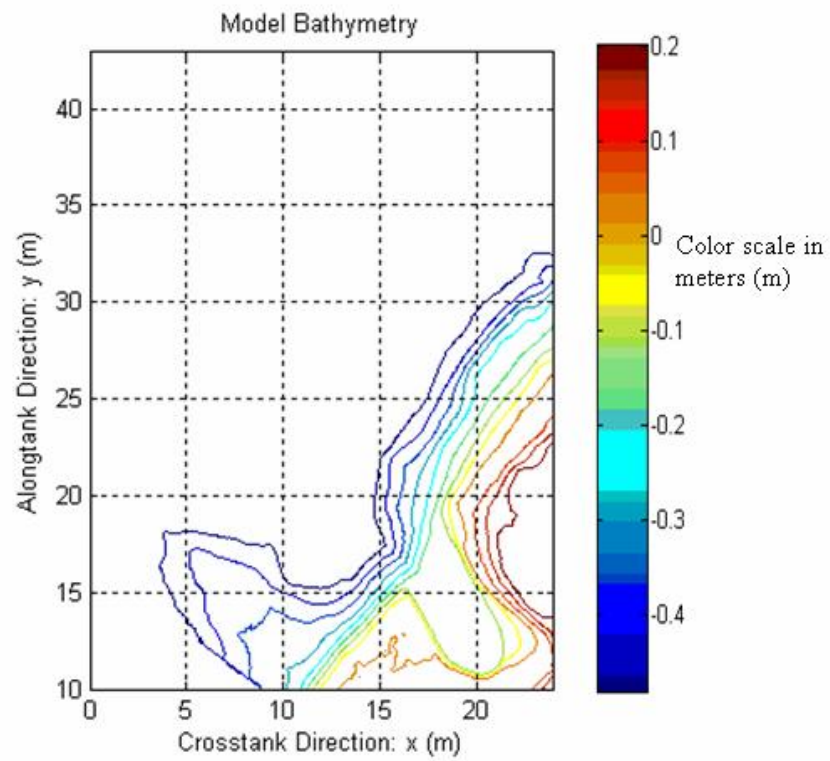


**Figure 8, Plot of survey data**

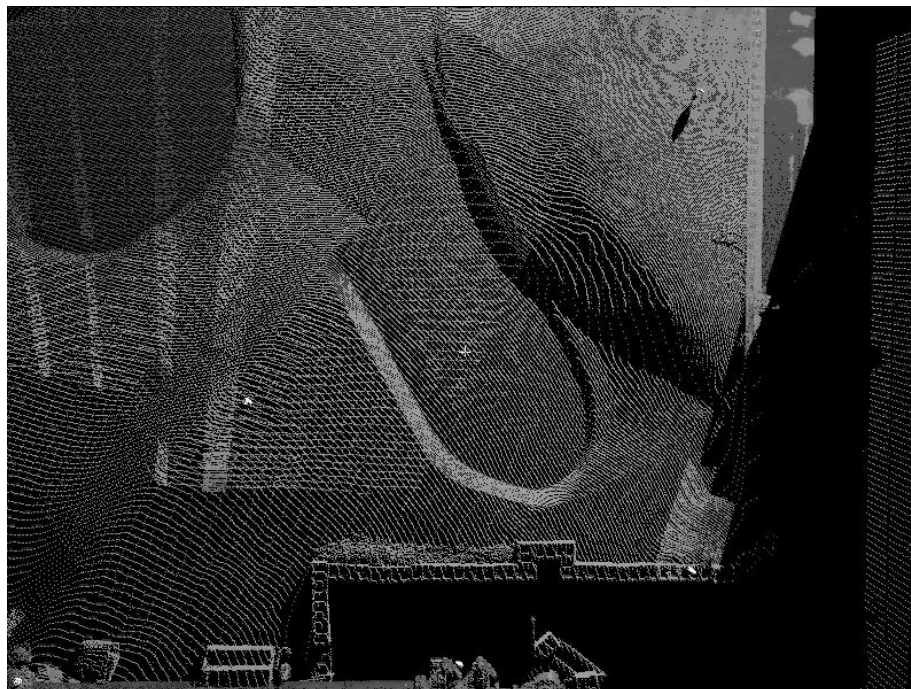


**Figure 9, Image produced from the LIDAR scan**

### 3.3 Modifications to existing model

To prepare the TWB for tsunami inundation testing this summer, several modifications to the model had to be performed. At the end of the extended CMU wall, a 1 on 10 plywood wedge with a metal tip was placed to avoid the effect of waves hitting a blunt object and reflecting waves into the test area. Figure 10a shows the CMU wall extension and figure 10b shows what the wedge looked like and how it was secured in place with several large lead weights.



**Figure 10a, Picture of extended wall**



**Figure 10b, Picture of wedge**

To ensure that the bathymetry was gradual at the foot of the model it was necessary to fill in an abrupt area. This region was filled with concrete, and given the same slope as the surrounding bathymetry. This filled in region can be seen in Figure 10a, where the plywood forms that were left in the finished concrete left wet marks where water leached out. This new region was manually surveyed in with a Nikon Pulse Laser total station and survey rod. This new survey data was incorporated into the existing 10cm bathymetry grid for the TWB. Figure 8 shows a plot of the model bathymetry using the completed survey data

## Chapter 4

### INSTRUMENTATION AND DATA ACQUISITION

#### 4.1 INSTRUMENTS

In order to collect the velocity, surface, and pressure measurements of the various cases, it was necessary to first learn how to properly use each instrument. Certain instruments required daily calibration, while others required no calibration at all.

##### 4.1.1 ADVs

Four Acoustic Doppler Velocimeters (ADV) were used for collecting water particle velocity of the incoming waves. The ADV made by SonTek/YSI is a single point, high resolution, three dimensional Doppler current meter. The ADV measures the velocity of the water by using the Doppler Effect. The transmitter portion of the ADV uses pulse-coherent processing technique to produce two pulses of sound at a known frequency, separated by a time lag. It then measures the phase of the return signal from each signal. This measured change in phase is then divided by the time between pulses. This time is directly proportional to the velocity of the particles in the water.

The ADV probe tips were kept at a depth of 10 cm below still water level (SWL) for the 55 cm depth, and 6cm below SWL for the 44 cm water depth. The sampling volume for the ADVs was located 5 cm below the ADV probe tips, and the sampling volume was centered at 4.5 mm below that. This positioned the ADV sampling volume at 15.45cm

below the SWL. Time series of velocity were collected at a 50 Hz sampling rate, starting about 20 seconds before generation of the tsunami and continuing for 60 s or 120 s depending on which case was run. This was determined to be the necessary time to capture the passing wave and any harbor wave interactions that took place.

For the ADVs to work properly, the acoustic energy must be reflected in all directions by the particulate matter contained in the water. Before testing started for this project the TWB was drained of the silt latent water remaining in the basin. This meant that an artificial seeding material was required to provide the reflecting particulate in the water. After several unsuccessful attempts to seed locally near the ADVs, it was decided that the entire basin would be seeded. The seeding material used was the SonTek recommended microscopic (11 micrometer diameter) clear hollow glass spheres. These microscopic spheres produced by Potter Industries Incorporated came in a dry powder form. This seeding material was essential for what we needed in that the product itself was split into some spheres that were more buoyant, less buoyant, and the same buoyancy of water. This meant that the seeding material would be evenly distributed through the depth of the water in the TWB. These microscopic spheres provided the particulate matter to sufficiently reflect the acoustic energy of the ADVs.

The actual seeding of the TWB was achieved through mixing the seeding material in five gallons buckets with TWB water, and then spreading it out in a pattern that evenly distributed the seeding mixture. Figure 11 shows the spreading out of the mixed seeding material.



**Figure 11, Spreading out the mixed seeding material**

The volume of the TWB at a depth of 55 cm calculated to be 550,000 liters. The concentration of the water in the basin after seeding an entire 53 lb bag was calculated out to 43.80 mg/L. This concentration fell into the range of 10-50 mg/L, which was the specified concentration called out for in the SonTek manual. Figure 12 shows the powder seeding material being mixed with fresh water from the basin. A respiration mask was used when handling the dry seeding material.



**Figure 12, Mixing the dry seeding material with fresh basin water**

#### **4.1.2 Wave gauges**

The wave gauges used for this experiment were of the resistance type, and for this experiment they were used to measure surface elevations along the longshore and cross-shore range. The wave gauges had a constant voltage, and as the water level rose the resistance was lowered, which in effect increased the current. This increase in current caused by the water surface increase was then run through a 1 ohm resistor, where the voltage in turn went up based on the theory of Ohm's Law. Ohms law seen below in equation 4.1, states that the resistance ( $R$ ) is directly proportional to the ratio of the voltage ( $V$ ) over the current ( $I$ ).

$$R = V / I \quad (4.1)$$

Therefore a measured increase in water surface corresponded to a measured increase in voltage. Through this concept, the wave gauges were calibrated by immersing the wave gauges a known distance in water and then recording the increase in voltage. After a series of these measurements, a linear calibration slope was acquired that allowed us to determine what the water surface elevation was. Due to the nature of the wave gauge equipment it was necessary to calibrate the wave gauges every 24 hours. The testing frequency used for the wave gauges was also 50 Hz, because the ADVs and wave gauges were used simultaneously and therefore had to be synchronized.

#### **4.1.3 Pressure sensors**

The pressure sensors used were of the strain gauge transducer type. These sensors show significant resistance change when they are strained. This change in resistance is related



to three effects. The first effect is caused when the length of conductor is changed it undergoes a resistance change that is roughly proportional to the change in length. The second effect, is that when the length of the conductor is changed, this causes a change in its cross sectional area and a resistance change that is roughly proportional to the change in area. The third effect is called the piezoresistive effect. This effect which is a characteristic of the material, and is a change in the bulk resistivity of a material when it is strained. Similar to the wave gauges, the pressure sensors were calibrated by lowering them a known distance into water and observing what the resultant change in voltage are. This process is repeated until a linear calibration curve is made, that shows a slope of voltage change to cm of water. Pressure sensors only have to be calibrated once. Figure 13 shows the calibration of the pressure sensors while they are already installed in the testing cylinder. This technique saved time, in that all of the sensors could be calibrated at the same time.



**Figure 13, Pressure sensor calibration**



## 4.2 Method of deployment

### 4.2.1 ADVs and wave gauges

The TWB came equipped with a mobile aluminum bridge that connected the North and South sides of the basin. This bridge was built on a set of large wheels that allowed it to move either East or West, and provided the ability for the bridge to cover the entire basin. To deploy the ADVs and wave gauges, it was necessary to construct a frame that attached to the bridge and extended close to the water. Figure 14 shows the bridge and the frame that we built onto it.



**Figure 14, Picture of frame on the bridge and frame**

The ADVs and wave gauges were then co-located on the I-beam that was positioned 30 cm above the SWL. Figure 15 shows how the instruments were mounted onto the I-beam. The wave gauges can be seen mounted to the left, and the ADVs are to the right. Both devices were secured to the I-beam using several C-clamps.

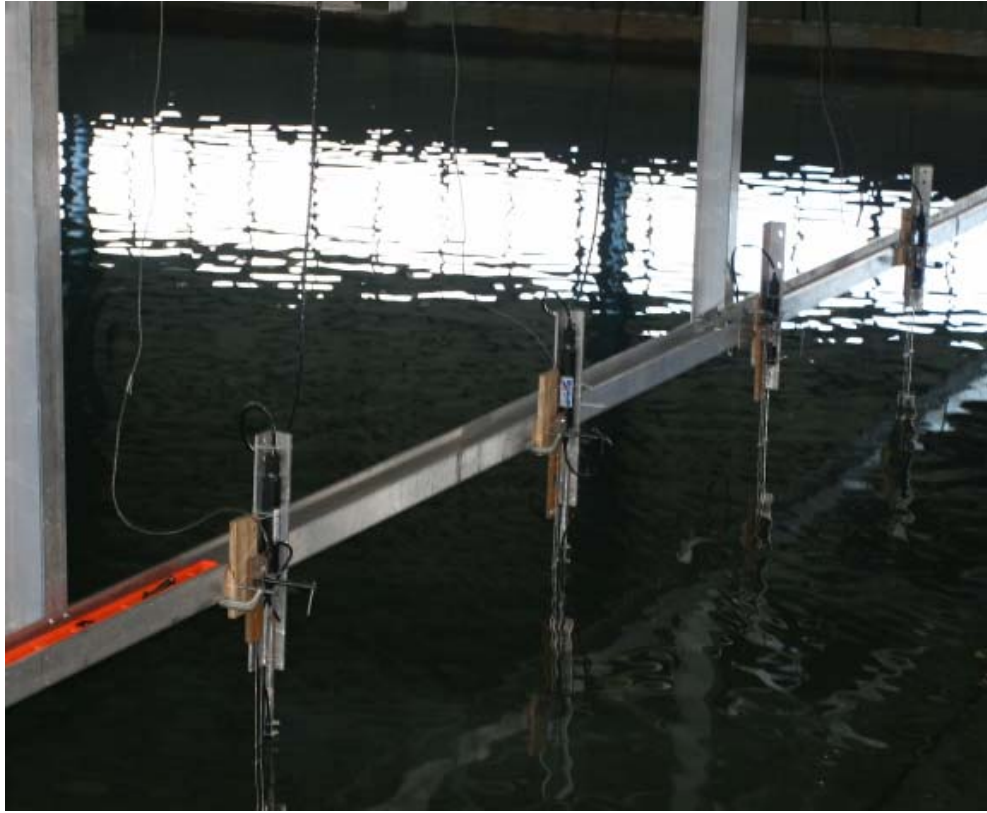


**Figure 15, Picture of 4 pairs of wave gauges and ADVs mounted on the frame.**

#### **4.2.2 Pressure sensors**

The mechanism for deploying the pressure sensors was the cylinders themselves. The pressure sensors were threaded into the wall of the cylinder, with the face of the sensor being flush with the outside of the cylinder wall. In Figure 16, four circles in the side of the cylinder can be seen, this is where the pressure sensors were threaded into the cylinder, with the actual sensor remaining inside the cylinder. Although four circles are shown, the top hole was filled due to the forth pressure sensor proving to be non-functional. All pressure testing was done with 3 sensors.

Two cylinders were used, one that was 46 cm long as seen below, and another one that was 26 cm long. The cylinders were marked with a black stripe every 5 cm. In the figure below, a sensor can be seen at 2.5 cm, 13 cm, and 26 cm. The other test cylinder not

shown in figure16 had the sensors located at 2.5 cm, 6 cm, and 12 cm. These sensor locations were chosen based on the wave conditions run.

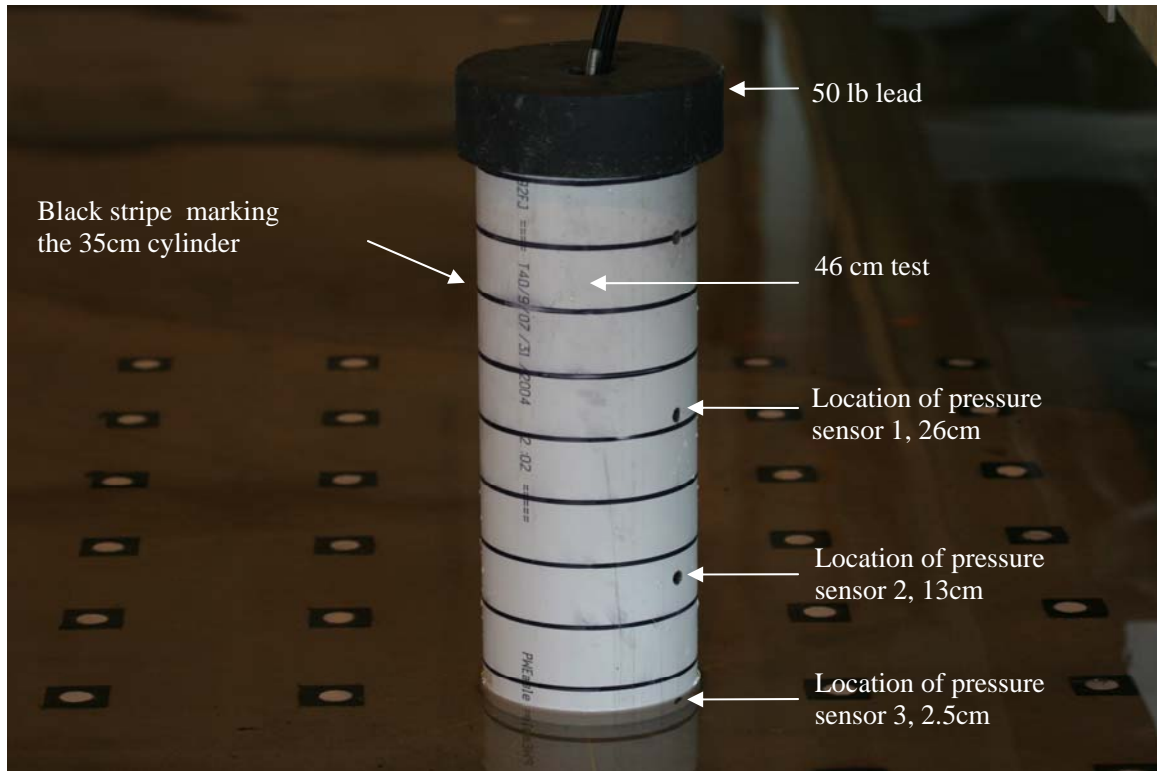
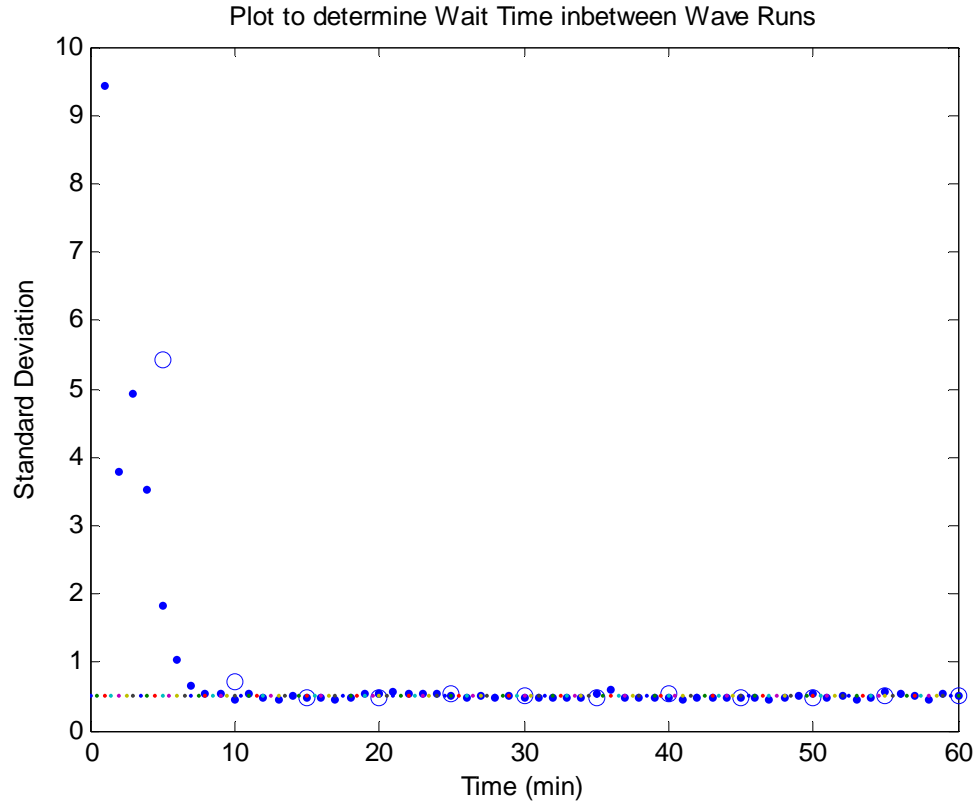


Figure 16, Picture of flush mounted pressure sensors, and 50lb top weight

### 4.3 Wait time between runs

Before testing could start, the time required to wait in between runs had to be determined. This was done by running a 25 cm wave and then leaving an ADV on for 60 minutes after the wave was run. In Figure 17 the open circles represent the standard deviation every 5 minutes and the solid circles represent the standard deviation every 1 minute. It can be seen that at the 10 minute point the water has reached a level of calmness that will not be noticeably improved after the first 10 minutes. Since this test was run with the largest of the cases, 10 minutes would be appropriate for the 25 cm wave, and conservative for all other cases.



**Figure 17, Plot of standard deviation taken at every minute vs. time. Taken from an ADV which was located in the center of the TWB at an offshore location, for the wave from case 1.**

#### **4.4 Repeatability level of velocity measurements**

Figure 18 show the superposition of three runs of the same wave condition. In recording this data, ADV 507 was placed in the same offshore location, while the wave-maker was given identical input to produce the same 25 cm wave. 10 minutes of wait time was provided in between all three identical runs. The second panel shows a magnification of the maximum velocity region, and the bottom panel shows a magnification of the lowest velocity region. For the area of interest, the maximum velocity region, the average for the three runs was 79.5 cm/s, and the standard deviation was 0.25 cm/s (31%). As seen from the plots in Figure 18 , the level of repeatability is acceptable.

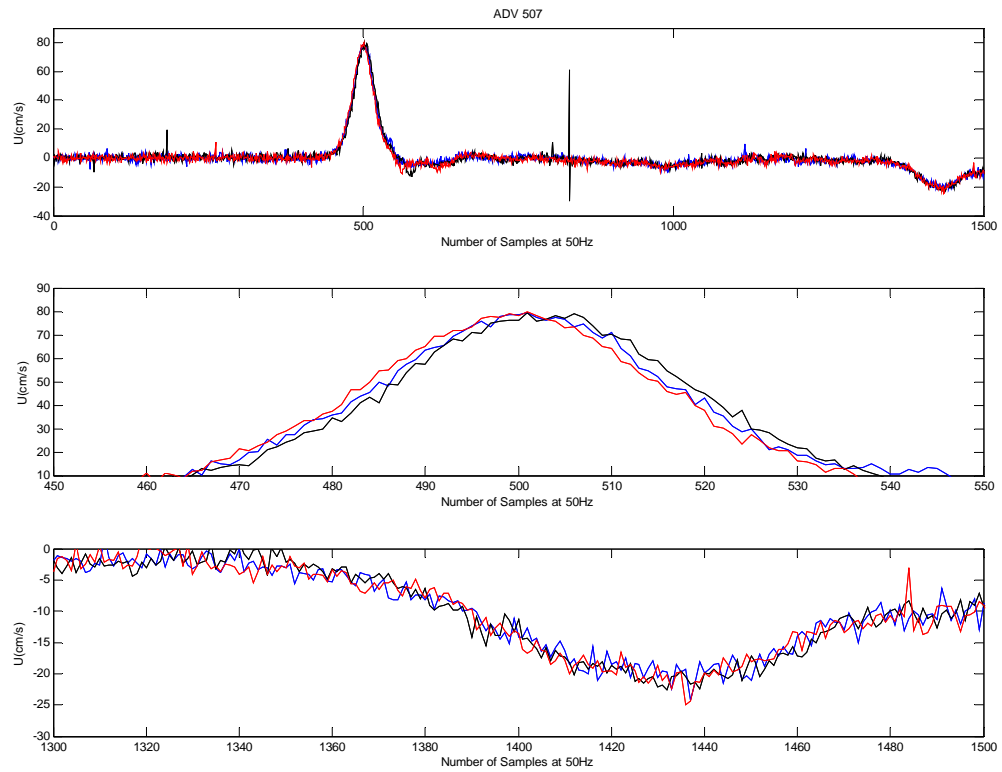


**Figure 18, Repeatability plots for the ADV**

## 4.5 Testing plan

### 4.5.1 Cases

Four cases were used for testing. The characteristics of these cases can be seen in table 2.

<b>Table 2, Case Types and Descriptive Parameters</b>						
case	d	Type	target H	observed H	H/d	N runs
-	(cm)	-	(cm)	(cm)	-	-
1	55	Soliton	25	22.69	0.41	25
2	55	Soliton	5	4.44	0.08	25
3	44	User defined		7.93	0.18	19
4	44	Soliton	5	4.51	0.1	19

Case 1 was chosen to model the scenario of a tsunami wave that has already broken offshore and produces a bore that enters the harbor. This allowed us to look at the impact forces caused by a bore on a cylinder. This bore producing wave demonstrated the typical observed tsunami condition of a wall of water approaching shore. Case 2 was chosen because it modeled the scenario of a non-breaking tsunami wave that breaks as it reaches the shore. Case 3 provided a tsunami wave that broke in the harbor, and used the larger stroke feature of the wavemaker. Case 4 provided a tsunami wave that breaks in the harbor, but has no overtopping of the physical model. These considerations given to the selection of the cases were, including how well the wave run-up was contained on the model, are explained in Ichikawa (2005).

Cases 1, 2, and 4 were generated using a solitary wave program that came with the MTS software. This equation for the wave board time, history which is used in this program, can be seen in equation 4.1 (Hughes, 1995).

$$X_o(t) = \frac{H_o}{\kappa d} \tanh \kappa(C^*t - X_o) \quad (4.1)$$

$$C^* = \sqrt{g(d + H_o)} \quad (4.2)$$

$$\kappa = \sqrt{\frac{3H_o}{4d^3}} \quad (4.3)$$

The variables  $X_o$ ,  $H_o$ , and  $d$  are the instantaneous wave board position, the offshore wave height, and still water depth at the wave board. The variable  $C^*$  is the shallow water wave celerity, shown by equation 4.2. The variable  $\kappa$  is explained by equation 4.3. The general idea of the shallow water wavemaker theory is to match the velocities of the waveboard to the water particles of the desired wave as the board moves. It is assumed

that beneath the long wave, the horizontal velocities are nearly constant over depth (Hughes, 1995).

Case 1, 2, and 4 were generated by a sudden and fast movement of the wavemaker paddles. This sudden displacement of case 1, 2, and 4 can be seen in figure 19, while figure 20 shows the resultant wave as measured by the wavemaker.

The wave for case 3 was generated using a programmed wave displacement file by Ichikawa (2005). The equation for this displacement file can be seen in equation 4.4.

$$Xo(t) = \frac{Disp}{2} erf\left(\frac{(t-t^*)}{2.75}\right) \quad (4.4)$$

*Disp* stands for the available displacement of the wavemaker. The total displacement available for the TWB wavemaker is 2 m, and 1.62 m was used because it gave a reasonable wave compared to cases 1, 2, and 4. The symbols  $t$  represents time, while  $t^*$  represents the time allowed for the wavemaker's forward displacement. The symbol *erf* represents the error function. The error function is what causes the symmetric, asymptotic shape of the wavemaker's displacement. The error function is commonly used to simulate the displacement as a function of time for a solitary wave. The constant of 2.75 was used to provide the slow rate of wavemaker movement during displacement. For case 3, the wavemaker paddles were set near their largest negative stroke, this was done to take advantage of the full stroke capacity of the wavemaker. Figure 19 shows the long, slow wave that was generated by case 3, and Figure 20 shows what the resultant wave looked like at the waveboard. For clarity the top panel 1 in Figure 19 shows all of the displacements beginning at  $x=0$ , when in reality they all started from a position with a negative waveboard displacement. The normalization process used for the lower panels

of figures 19 and 20 involved dividing all the values for each case by the largest value of waveboard displacement or wave height in each case.

From the normalized plots in Figure 19 and Figure 20 it can be observed that case 3 has a different wave shape and a much larger wavelength than the other cases.

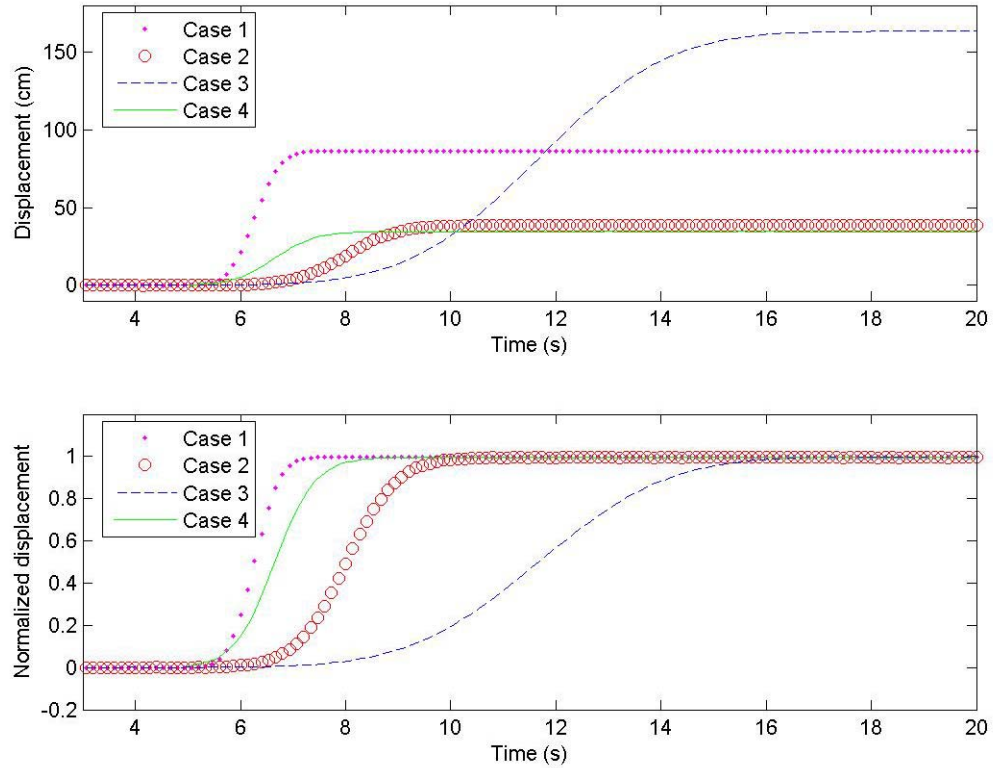


**Figure 19, Solitary wave control signal showing the displacement of the waveboard**



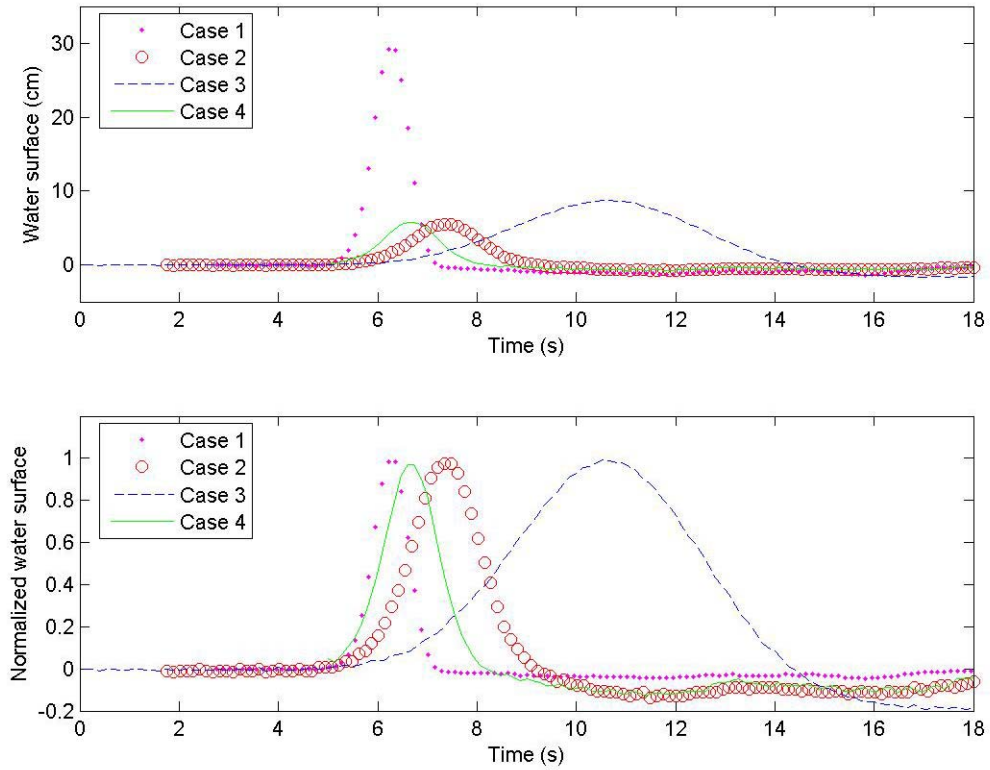


**Figure 20, Incident water surface elevation at the wave board**

## **4.5.2 Wave gauges and ADVs**

### **4.5.2.1 Testing locations**

In order to test water elevation and particle velocities over most of the TWB, it was decided that the basin would be divided into three regions of interest. The offshore portion of the model was divided into a north and south half. These two regions had ADVs and wave gauges spaced every 2 m in the alongshore direction. The third region covered the harbor and had the ADVs and wave gauges spaced every 1 meter. The harbor region was not tested for the offshore water depth of 44 cm because the harbor was too shallow for the ADVs. Figure 21 and Figure 22 show the testing grids that were

used for collecting all water surface and particle velocity data. The north testing locations are identified by red circles, the south testing locations are identified by green circles, and the harbor testing locations are identified by blue circles.

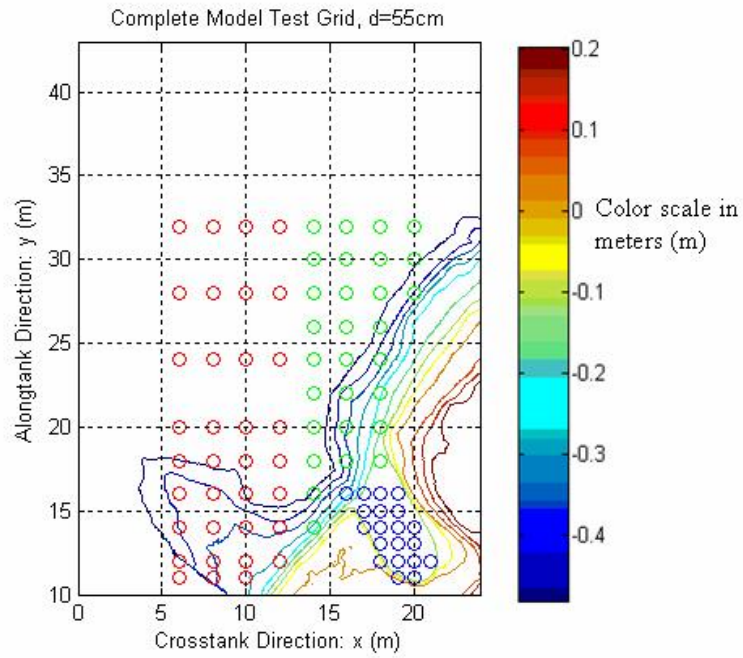


**Figure 21, Testing locations for WGs and ADVs, for offshore depth of 55cm, Cases 1 and 2**

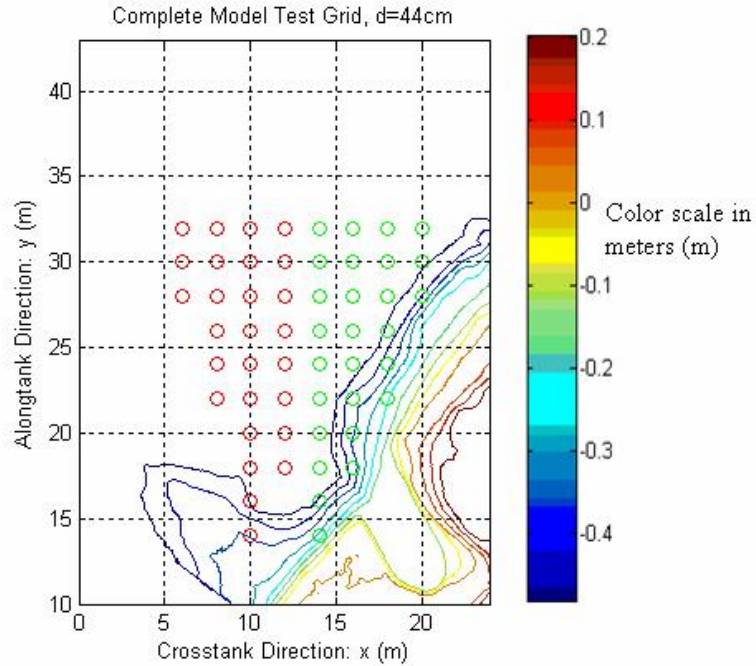


**Figure 22, Testing locations for WGs and ADVs, for offshore depth of 44cm, Cases 3 and 4**

#### **4.5.2.2 Data acquisition**

During testing, the time to take each run was about 12 minutes. The actual data acquisition was the first 2 minutes of the run, while the last 10 minutes were allotted for the water in the TWB to return to ambient still water conditions. During this 10 minutes, other tasks such as resetting the wavemaker, inputting the new wave condition, moving the bridge to the next testing location, and saving the data acquired from the last run were performed. To ensure accuracy with the bridge position, measurements were made to the nearest millimeter to the east and west of the previously measured meter increment marks that served as general crosstank location references.

The ADVs and wave gages were synchronized to take data simultaneously; however, the wavemaker ran separately. Although the wavemaker ran separately, there was a channel that recorded the wavemaker displacement and initial output. This wavemaker output

was synchronized with the time history recorded by the ADVs and wave gauges.

Portable handheld bi-directional radio transceivers were used to communicate between the data acquisition operator on the bridge and the wavemaker operator in the control room. It is noted that cases 1, 2, and 4 acquired key parameter data between 20 and 40 seconds of the 2 minute acquisition period. Case 3 acquired the key parameter data between 40 and 80 seconds of the 2 minute acquisition phase. Key parameters to be considered are maximum wave height and maximum horizontal wave velocities. Figure 23 through Figure 26 show the surface profiles and velocities measured at 4 adjacent offshore locations.

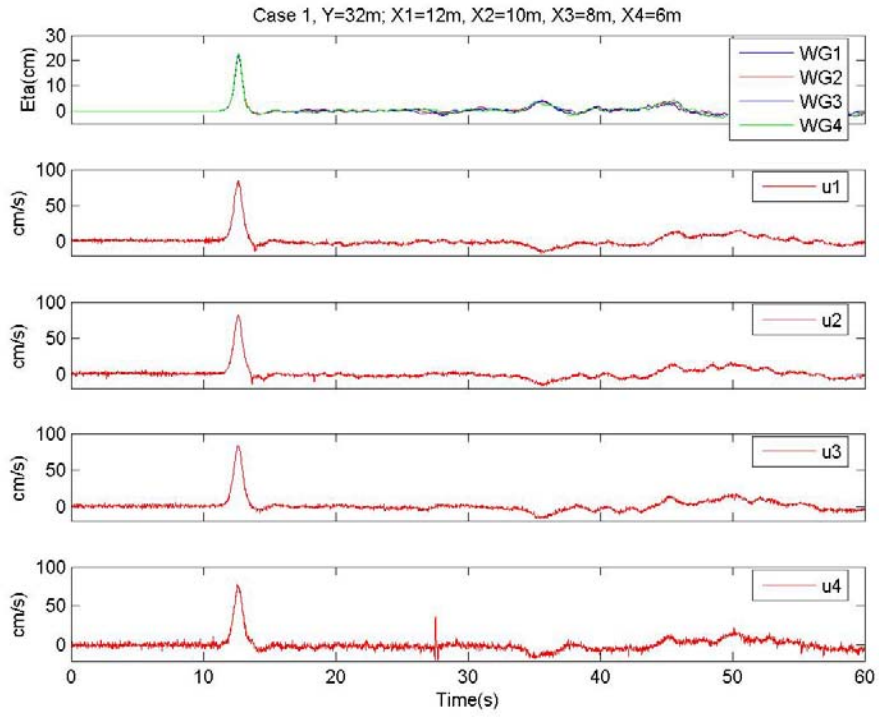


**Figure 23, Plots of raw data from WGs and ADVs for case 1.**

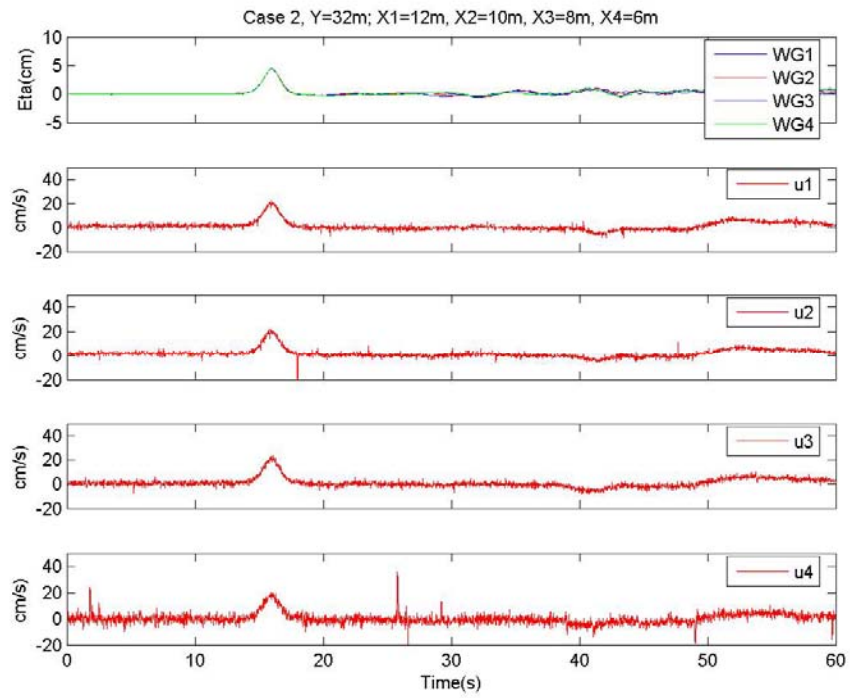


**Figure 24, Plots of raw data from WGs and ADVs for case 2.**

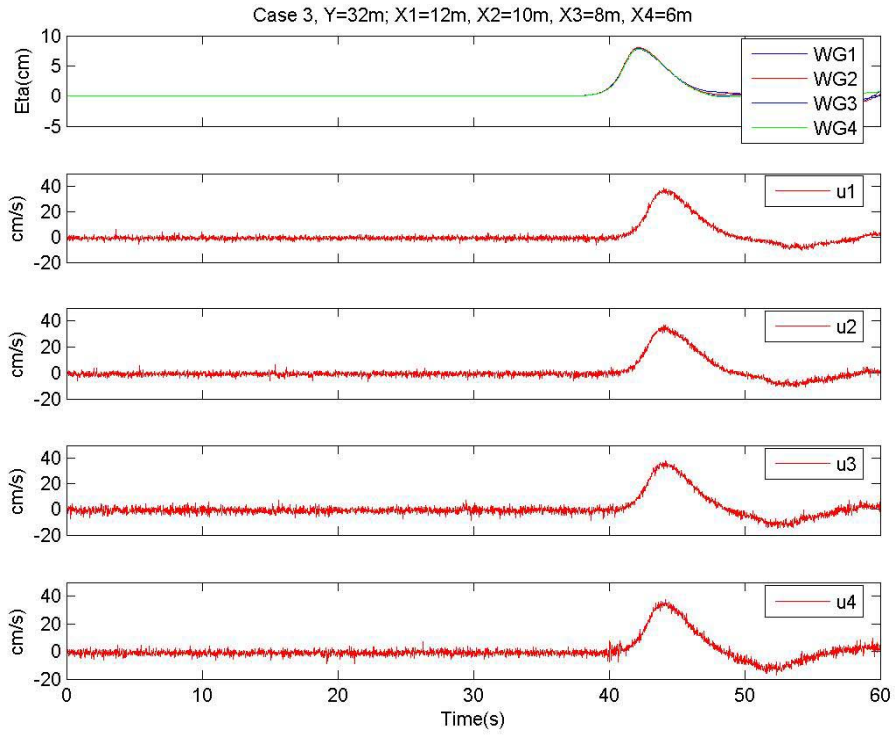


Figure 25, Plots of raw data from WGs and ADVs for case 3.

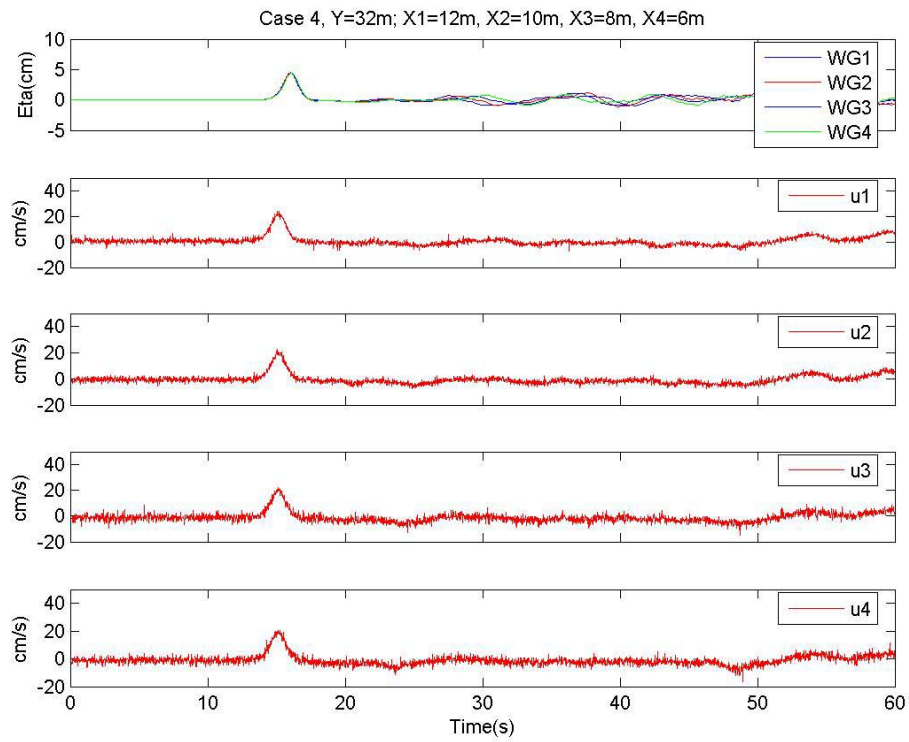
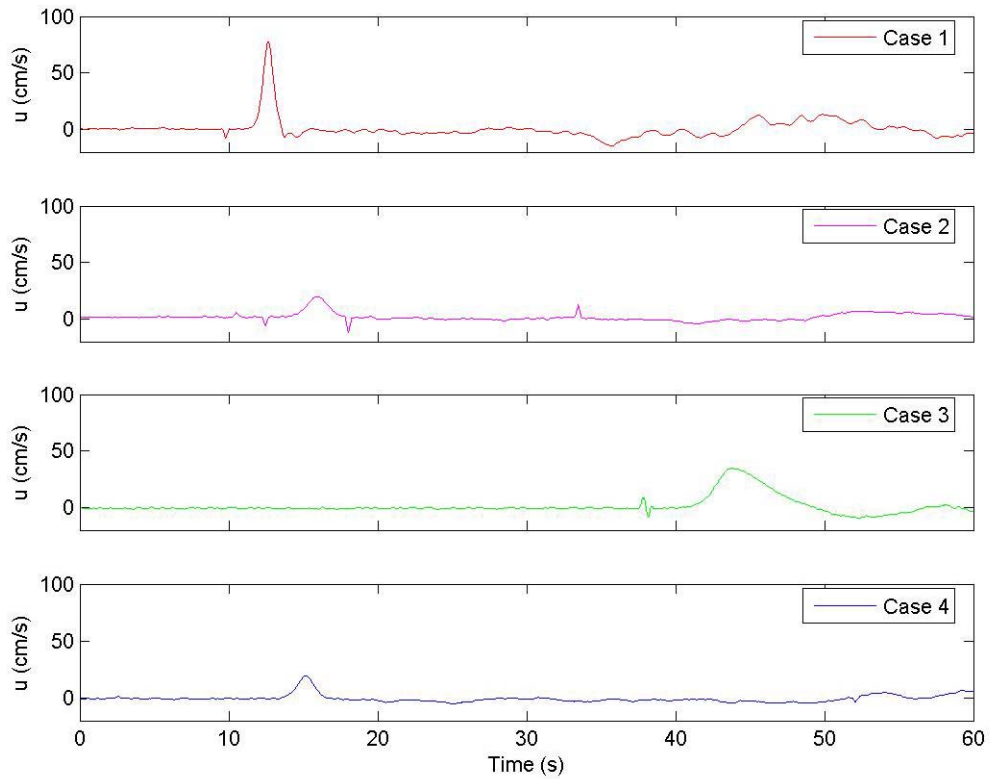


Figure 26, Plots of raw data from WGs and ADVs for case 4.

It can be seen from Figure 23 through 26 that the pattern of the water displacement is very similar to the pattern of horizontal velocity for each case. Figure 27 shows a comparison of the horizontal water velocity produced by each case as they pass the same offshore location. Case 3 has a velocity peak occurring later because the displacement program that produces it has a built in wait time before wave generation starts. From Figure 27, it can be observed that cases 1 and 3 which have the larger ratios of  $\frac{H_o}{d}$ , also have the steeper horizontal velocity profiles.



**Figure 27, Comparison plot of the horizontal velocities produced by each case, measured at the same offshore location.**

#### 4.5.3 Pressure sensors

#### 4.5.3.1 Testing locations

Figure 28 shows the locations where the cylinder, containing the flush mounted pressure sensors, were positioned in the harbor. These locations were chosen because they covered the main regions of interest for the harbor, mainly the mouth of the harbor, and the back of the harbor.

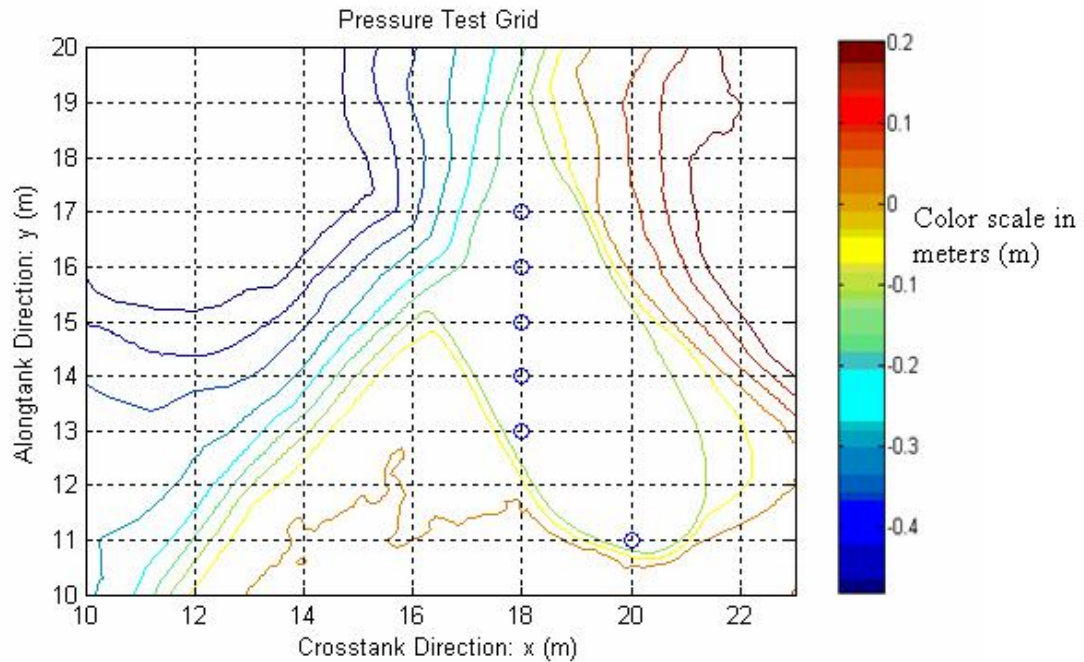


**Figure 28, Pressure Testing Grid**

The location of  $x=18$ , and  $y=16$ , near the front and center of harbor, had the most tests performed. This location was selected for the most intensive testing because it coincided with the location where the wave broke (case 4), and the location seaward to wave breaking (case 3). Like all other locations in the harbor, case 1 was already a broken wave at this location, and case 2, which breaks at the still water shoreline, represented the



non-breaking wave for this location. Table 3 describes the types of testing performed at each location, and the cases tested at each location.

**Table 3, Pressure Impact Tests Performed, and Cases Run**

<b>Harbor location (m)</b>	<b>30 degree increments tested</b>	<b>Additional Ho = 10cm, 15cm, and 20cm tested</b>	<b>Cases tested</b>
x=11, y=17	normal only	-	all
x=18, y=17	normal only	-	all
x=18, y=16	yes	yes	all
x=18, y=15	normal only	-	all
x=18, y=14	normal only	-	all
x=18, y=13	normal only	-	all
x=20, y=11	normal only	-	all
x=19, y=13	normal only	-	3, 4

#### **4.5.3.2 Data acquisition**

Due to limitations on the availability of testing equipment, the pressure testing was performed after the wave gauge and ADV tests. Since all pressure testing involved cases similar to cases 1 through 4, the same 10 minute settling time was used. Due to the sudden impact and nature of pressure impact testing, it was decided to use a higher frequency of 15 kHz. This is similar to the 12 kHz testing frequency used by Wienke and Oumeraci in 2004, when they performed tests of breaking waves acting on a slender cylindrical pile (Oumeraci, 2005).

Pressure sensor data was recorded in a similar manner to ADV and wave gauge data, in that the wavemaker output was recorded on a channel that was synchronized with the channel that recorded the pressure time histories. Key parameters to be considered are the maximum pressure impacts and the subsequent pressure history after impact of the wave. Figure 29 through 32 are examples of raw pressure time series taken for each case at the same harbor location, and with the pressure sensors oriented directly normal to the

wavemaker. Raw data was converted by the DAQ from volts to the pressure unit of cm of water.

The raw data of the pressure time series were examined to confirm that pressure spikes were not the result of noise. Figure 33 and 34 show the same plots shown in Figure 29 and 31, but the maximum values of pressure are closely examined to ensure accuracy.

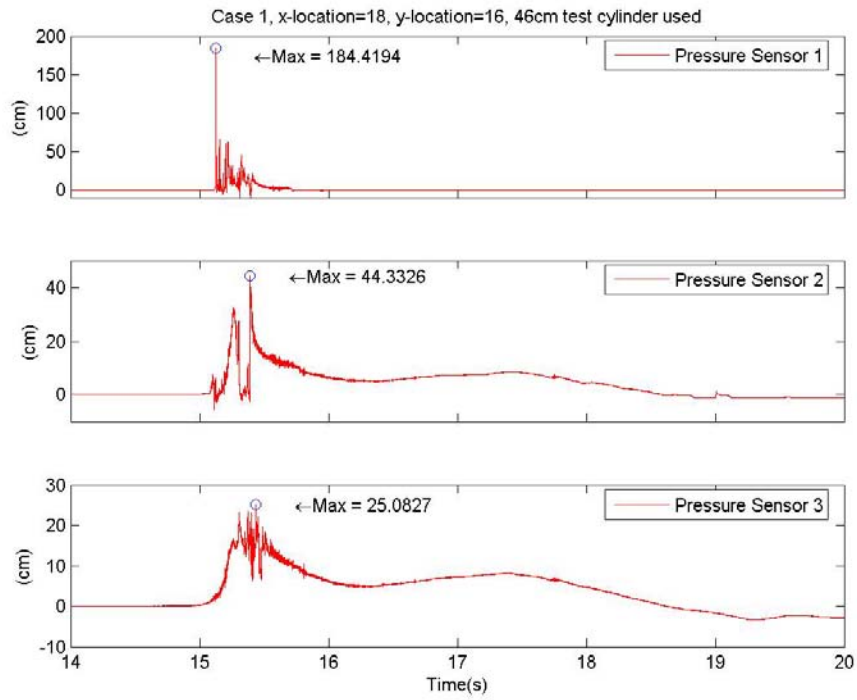


**Figure 29, Pressure time series for case 1**

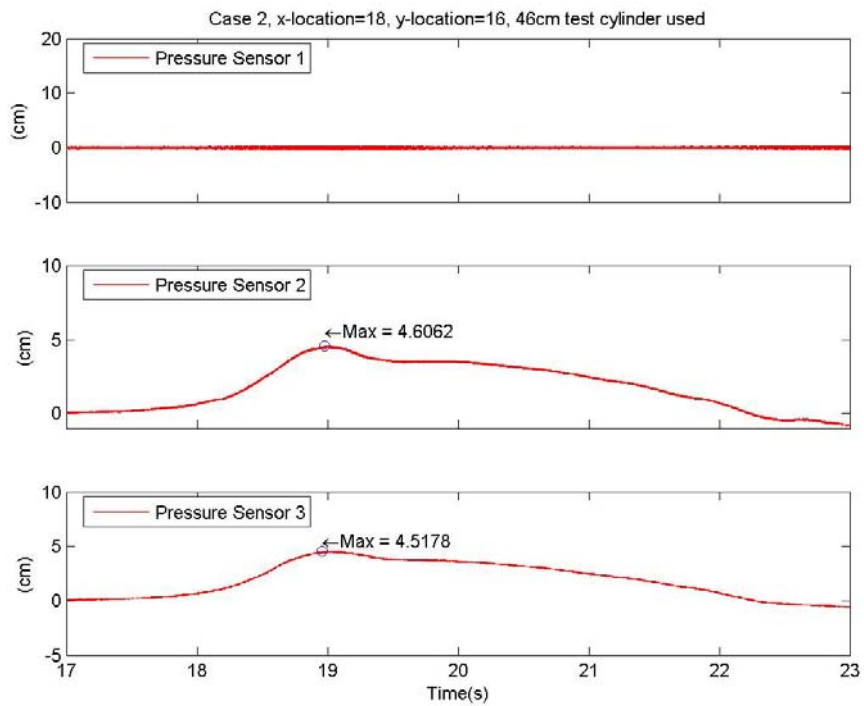


**Figure 30, Pressure time series for case 2**

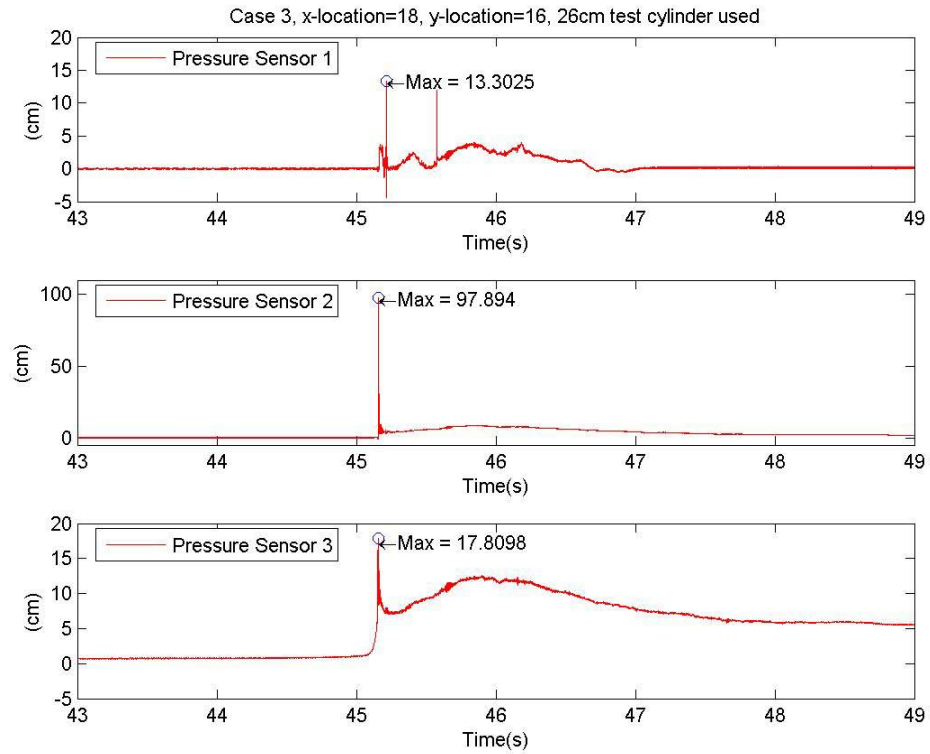


**Figure 31, Pressure time series for case 3**

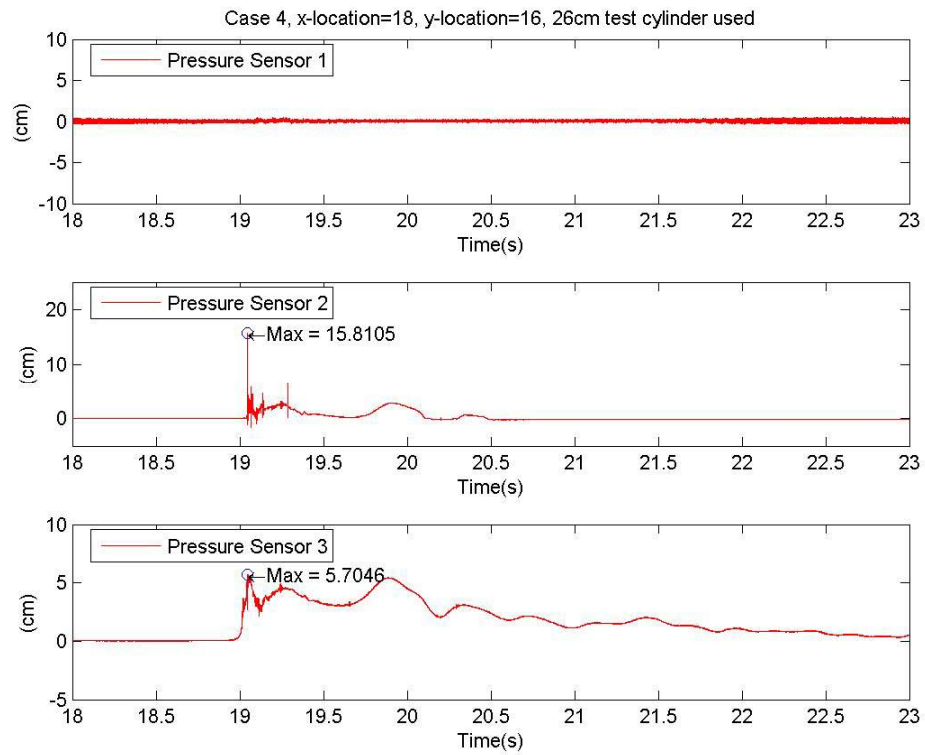


**Figure 32, Pressure time series for case 4**

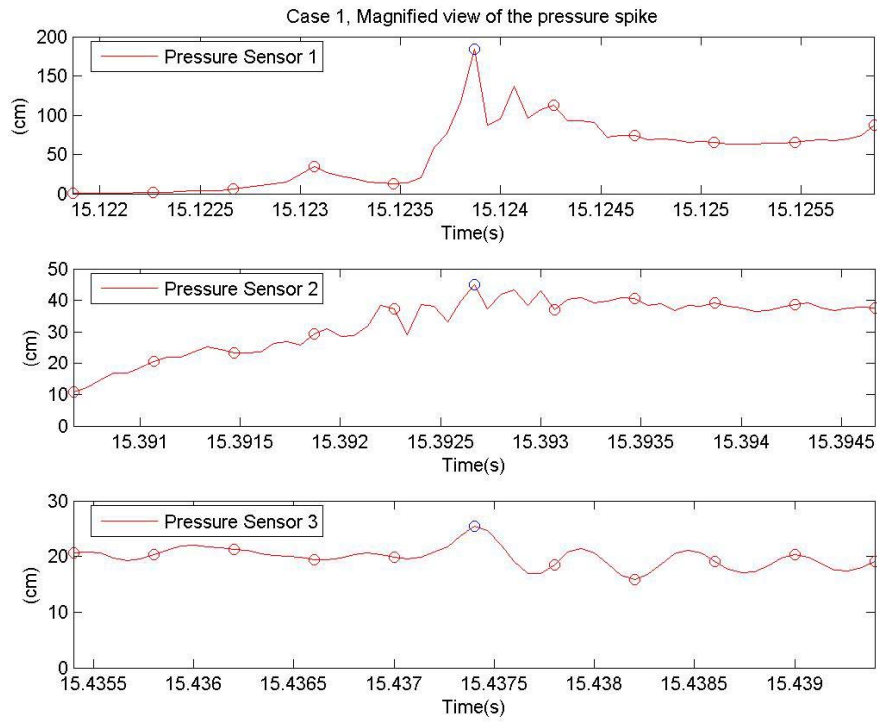


**Figure 33, Magnification of pressure spike for case 1**

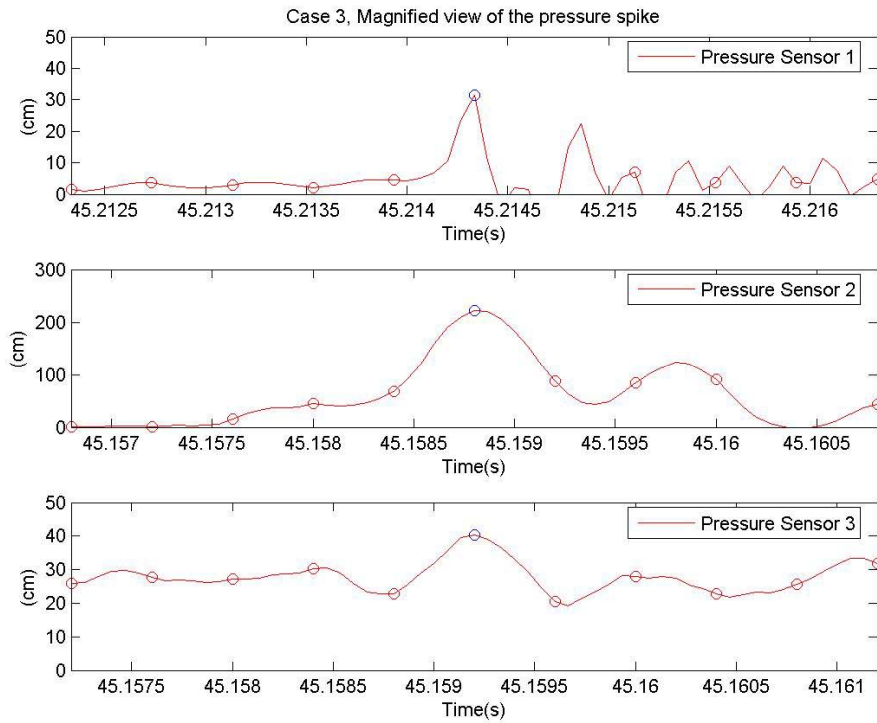


**Figure 34, Magnification of pressure spike for case 3**

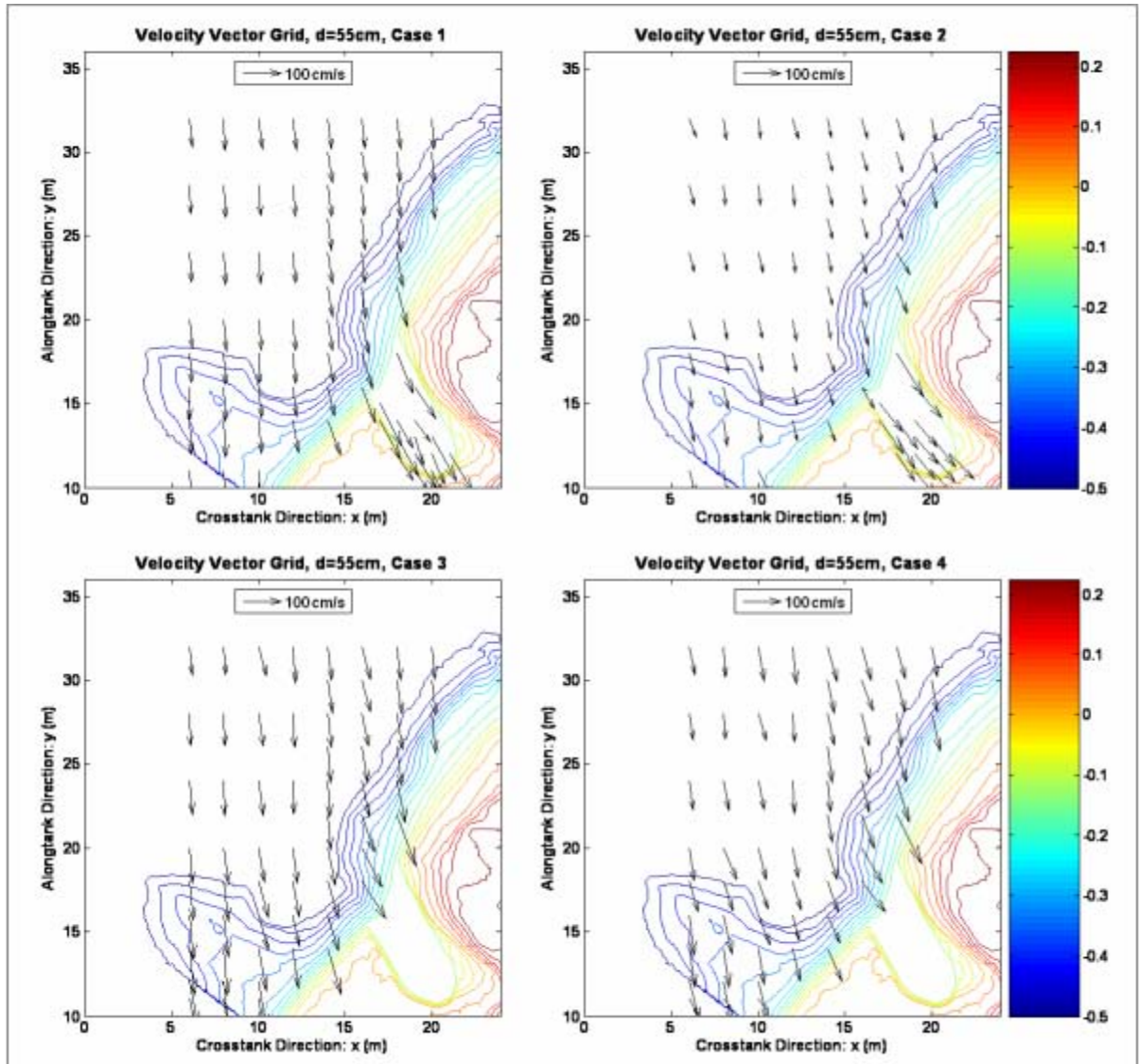
As seen from figures 33 and 34, which is a magnification of the pressure spikes for cases 1 and 3 shown over a range of two hundreds of a second. This might not seem like a large magnification, but the large sampling rate of 15,000 samples per second must be kept in mind. Overall it can be seen that the pressure spikes seen for cases 1 and 3 are not the products of noise or bad data collection.

## Chapter 5

### RESULTS

#### 5.1 ADVs

As a result of collecting water particle velocities at many points spread out through the TWB, it was possible to make velocity vectors plots for each case. It should be noted that the full data collection time frame, one minute for Cases 1 and 2 and two minutes for Cases 3 and 4, is displayed. Figure 31 shows the velocity vector fields for cases 1 through 4 are shown. Case 1 and 2 horizontal velocity vector flows are presented for the north, south, and harbor regions of the basin. Case 3 and 4 maximum horizontal velocity vector flows are presented for the north and south regions.



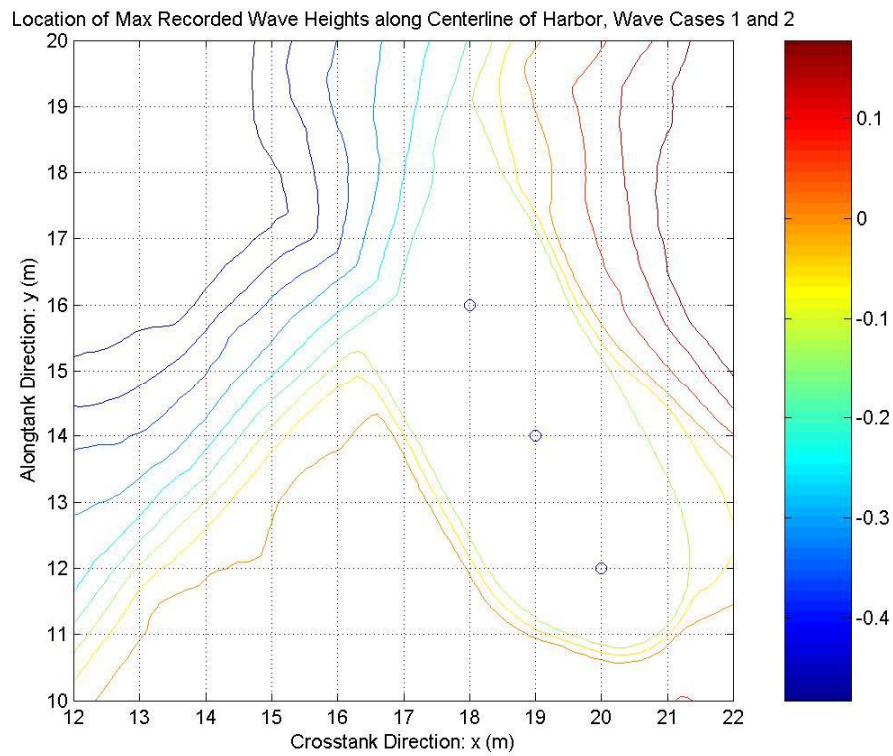
**Figure 35, Vector Plots of Maximum Velocity**

Figure 35 shows the process of wave refraction, where the velocity vectors representing the direction of the horizontal velocity are observed to turn towards the shoreline. All of the cases were generated with an offshore wave that approached the harbor entrance at an angle, but as seen from Figure 35 each case is redirected through refraction in a heads on direction as they enter the harbor.



## 5.2 Wave gauges

Through the collection of water surface elevations collected as a time series we were able to capture the maximum wave heights at each location tested. From the harbor wave gauge measurements made for cases 1 and 2, plots of maximum wave height as the wave enters the harbor can be plotted. Figure 36 shows the harbor locations of the wave heights as seen in Figure 37.



**Figure 36, MATLAB Plot Showing 3 Wave Gauge Points along the Centerline of the Harbor**

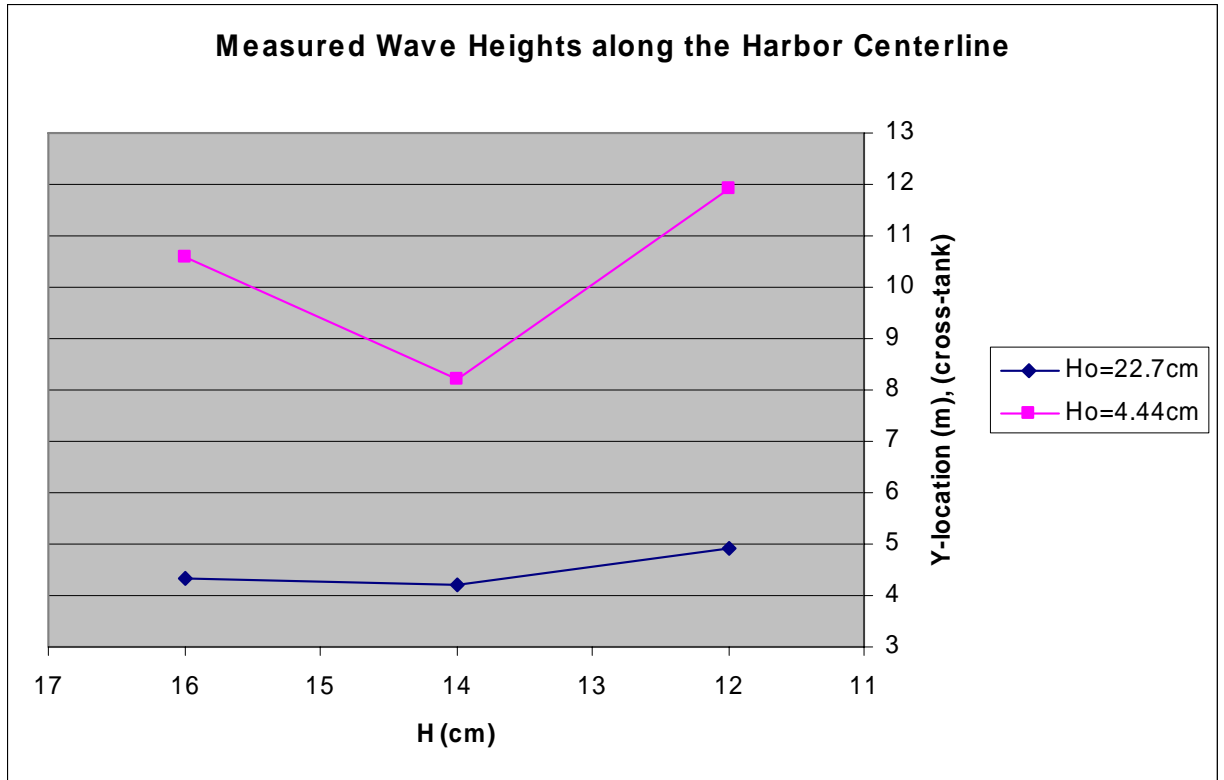
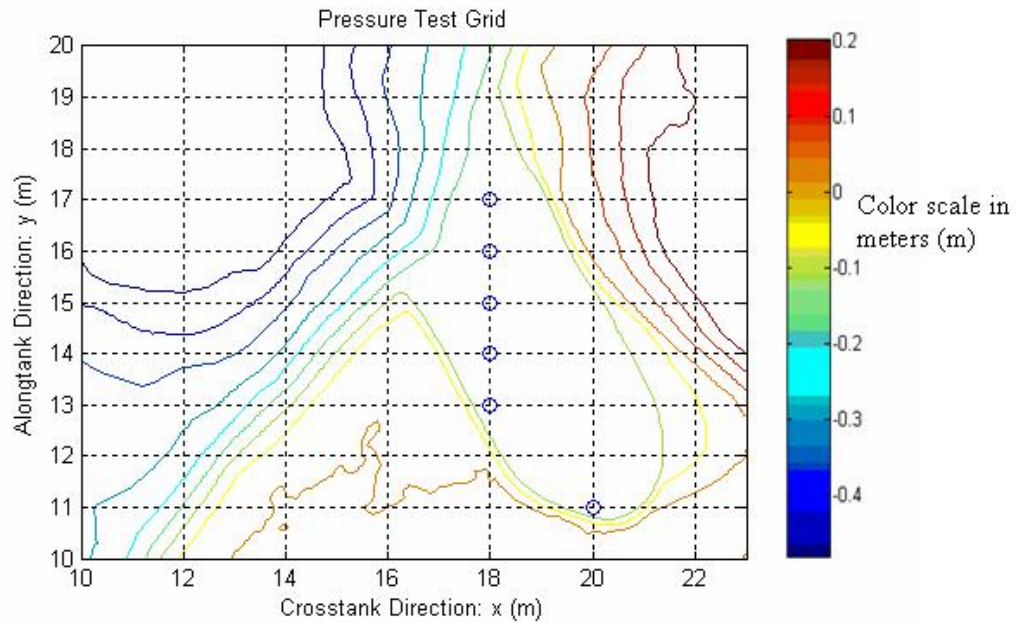


Figure 37, Measured Wave Heights for Cases 1 and 2

As seen from the graph in Figure 37, the wave heights both decrease as they enter the middle area of the harbor, but also increase as they enter the back region of the harbor. This trend is much more pronounced in the larger 22.70 cm wave. Most likely the waves increase in size as they first enter the harbor due to shoaling and the fact that the water is being throttled through the narrow entrance of the harbor. The waves then increase again in the back of the harbor due to the throttling effect of the waves being forced into the decreasing width of the back harbor. The fact that both the 4.44 cm (case 2) and the 22.70 cm wave (case 1) decrease in the center of the harbor is not fully understood.

### 5.3 Pressure sensors

Figure 38 shows the testing locations used during pressure testing. Figure 39 shows the empty TWB, with the cylinder placed near the front of the harbor. The blue arrow furthest to the left marks the 0 degrees orientation, which was normal to the wavemaker.



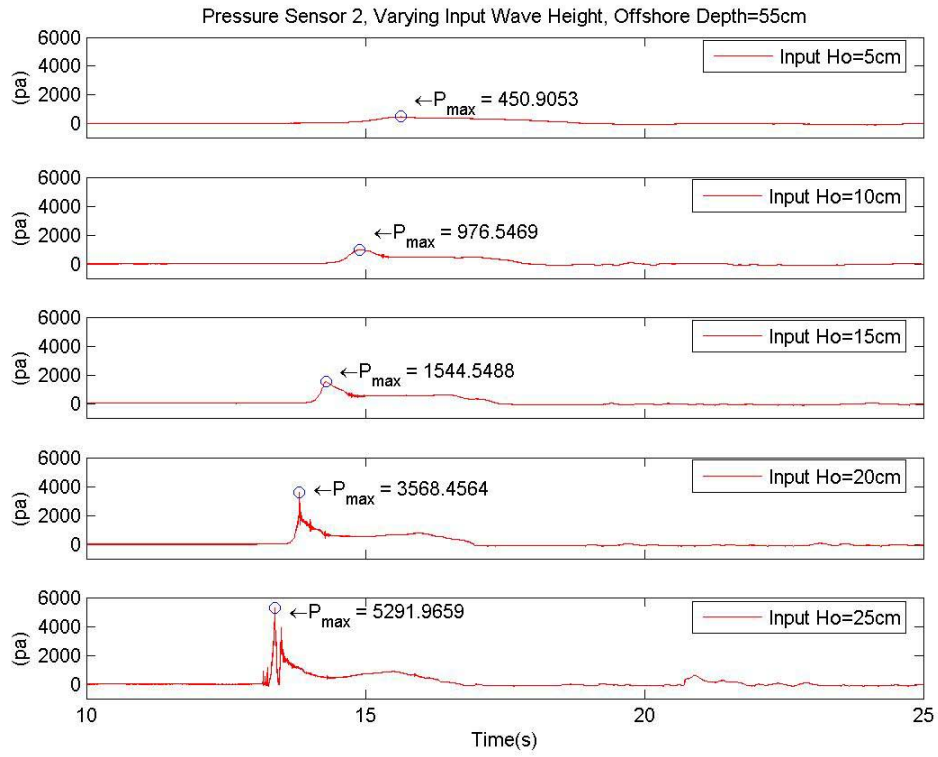
**Figure 38, Locations used for pressure-cylinder tests**



Figure 39, Picture of dry harbor with cylinder in the harbor location of  $x=18$  m,  $y=16$  m.

### 5.3.1 Varying wave height

Figures 40 and 41 show the pressure time histories caused by increasing input tsunami wave heights. The wave heights shown in the plots are the wave heights input into the wavemaker, the actual wave heights produced will be slightly smaller. These pressures were taken on the 46 cm cylinder, where pressure sensor 2 was located at 13 cm off of the harbor floor, and pressure sensor 3 was located at 26 cm off of the harbor floor.



**Figure 40, Pressure Time Histories for Increasing  $H$  at Pressure Sensor 2**

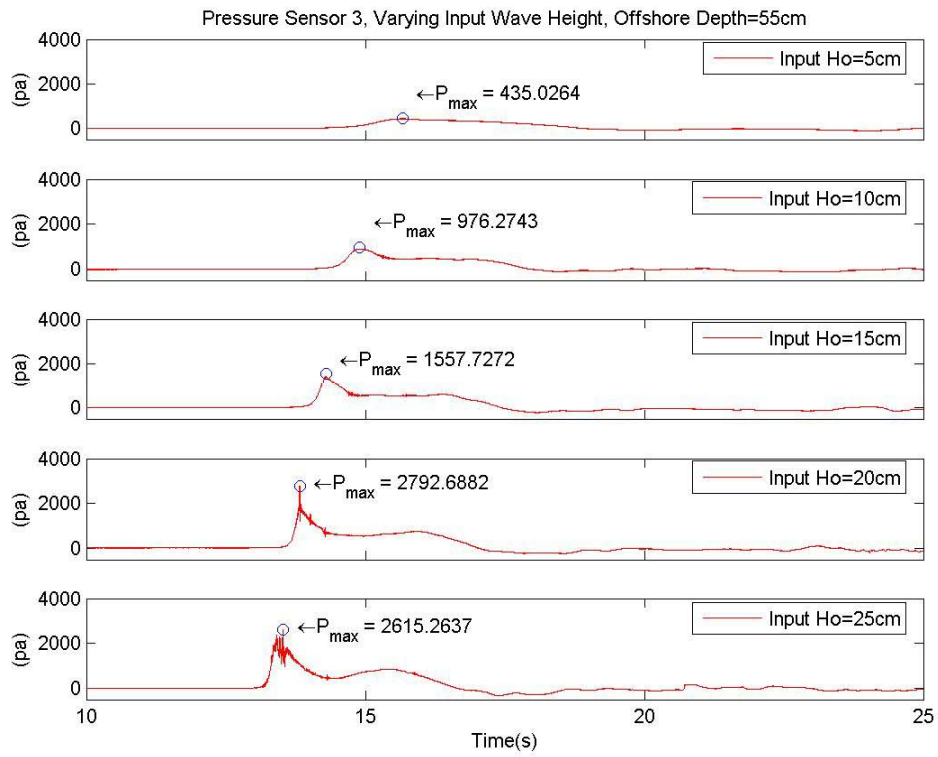


**Figure 41, Pressure Time Histories for Increasing  $H$  at Pressure Sensor 3**

The trends seen from figures 40 and 41 are that as the wave height increases for the tsunami wave, the wave reaches the cylinder in less time. This change in wave celerity is less as the wave heights are increased.

Another similar trend is the expected concept that the maximum pressures on the cylinder increase as the wave heights increase. The increase in pressure seen with each successive increase in wave height is less, as the wave heights increase. This is due to the fact that going from a 5 cm wave to a 10 cm wave, the wave height is doubled. Going from a 15 cm wave height to a 20 cm wave height is only a 25% increase, and therefore the pressure does not increase as much.

For both Figure 40 and 41, a large pressure spike can be seen in the pressure time history for the 20 cm wave. This is due to the fact that this wave has a steep face unlike the previous waves, and will impact the cylinder similar to that of a breaking wave. The pressure spike which acts over a short time is referred to as the “slamming” component. Wienke and Oumeraci break up the impacts of a breaking wave into two components, a quasi-static component which acts over a short time and is dependent on the breaker front and impact area, and a dynamic component that is seen for non-breaking waves.

(Oumeraci, 2004)

The 25 cm wave pressure time history, case 1, is different than the smaller wave heights due to the fact that this wave is already broken before it reaches the cylinder. The chaotic nature of the broken wave can be seen by the fact that at pressure sensor 2, the maximum pressure is almost double the maximum pressure value at pressure sensor 3. This would lead to the conclusion that the tumbling bore hitting the cylinder is very non-uniform in its horizontal velocity along the depth of the wave.

### **5.3.2 Varying y-location (crosstank)**

Testing was also done to see how the pressure time histories and maximum pressures would change as the test cylinder was moved towards the back of the harbor in the crosstank direction. Figure 38 shows the testing locations that were used. The alongtank x-location was kept constant at 18, while the crosstank y-location was decreased from 17 to 13.

#### **5.3.2.1 Case 1**

As expected the time until impact increases each time the cylinder is moved further back in the harbor. In figure 42, a large maximum pressure can be seen, as this cylinder location is shortly after the breaking point for case 1. The trend of the short duration pressure spikes can be seen to steadily reduce from the y=17 through the y=15 locations. At the y=14 through the y=13 location, the turbulent bore of the broken wave can be seen to level out. The difference between the maximum pressure at y=14 and y=13 is small overall, and it can be assumed that from this point on the bore has steadied in its shape and impact pressure.

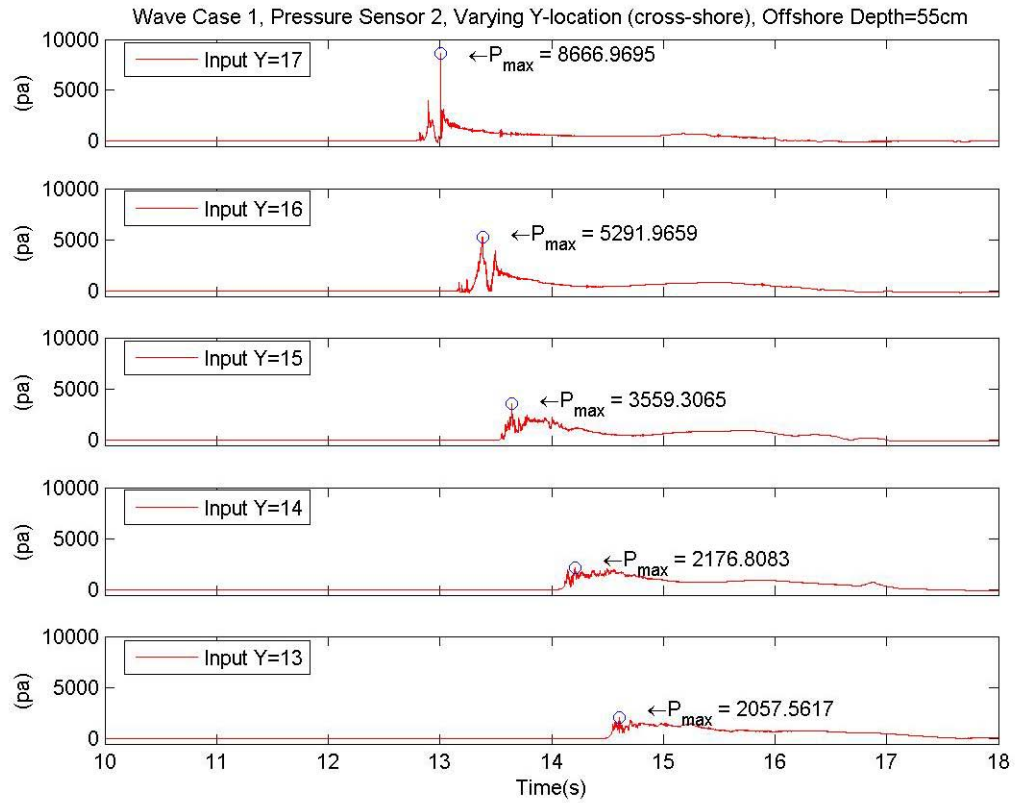


**Figure 42, Pressure time histories for increasing cross-shore distance at pressure sensor 2**

Figure 43 shows the pressure time histories, taken at pressure sensor 3, near the bottom of the cylinder. The plots in figure 43 do not show the same drastic decrease in maximum pressures as the cylinder is moved towards the back of the harbor. This low variance in the maximum pressure seen near the bottom of the cylinder can be partially attributed to the fact that the lower portion of the bore below the SWL is not as turbulent as the area of the bore at the SWL.



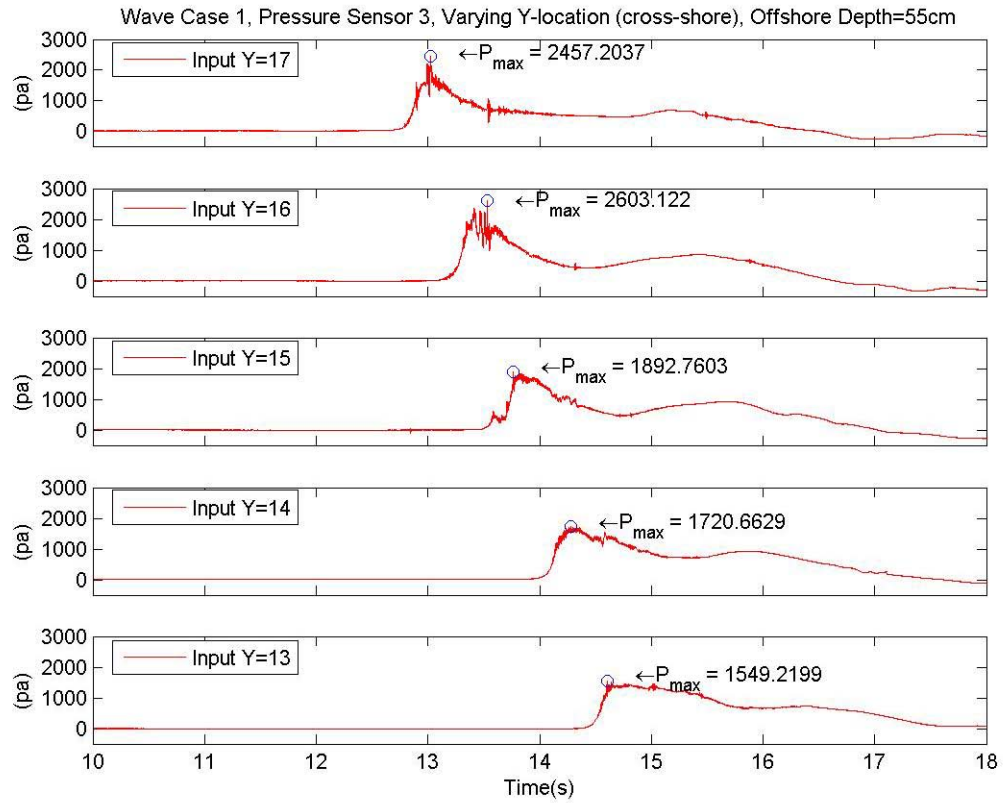


**Figure 43, Pressure time histories for increasing cross-shore distance at pressure sensor 3**

### 5.3.2.2 Case 2

Figures 44 and 45 show the pressure time histories of case 2, as the cylinder crosstank position is decreased. Overall the pressure time histories and maximum values are seen to not change much as the test cylinder is located further back in the crosstank direction. The largest maximum pressure values are seen at  $y=16$  and  $13$ . The  $y=16$  location corresponds to about a meter directly shoreward of the harbor entrance. At this location, the wave is now larger because it has been forced into the harbor entrance. At  $y=13$ , the wave has started to enter the narrow back of the harbor, and is increasing in size. This increase is observed in the higher pressures seen at  $y=13$ .

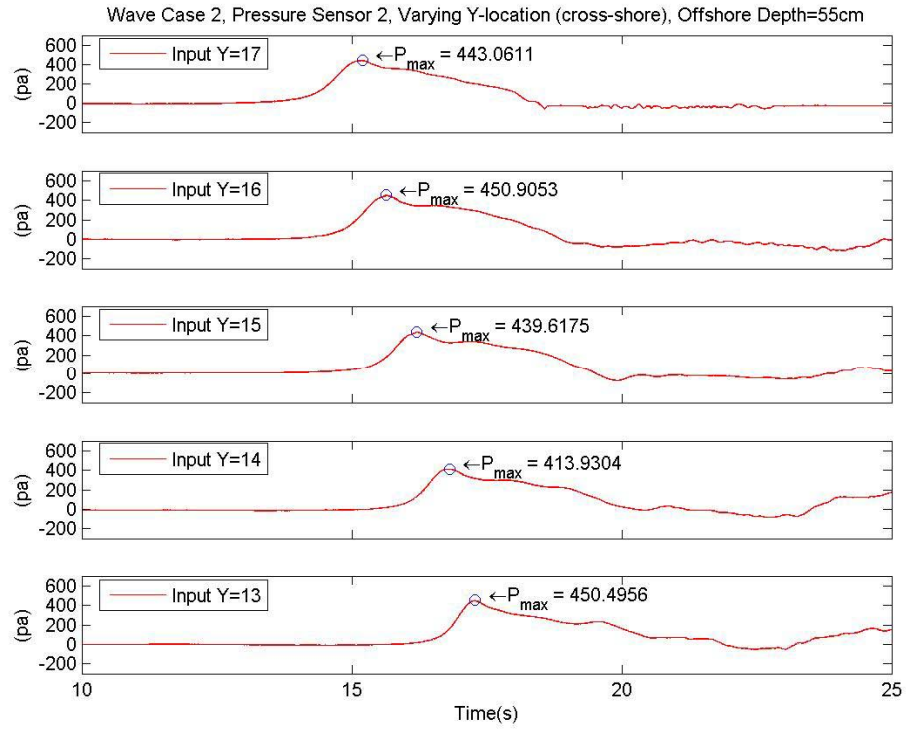


Figure 44, Pressure time histories for increasing cross-shore distance at pressure sensor 2

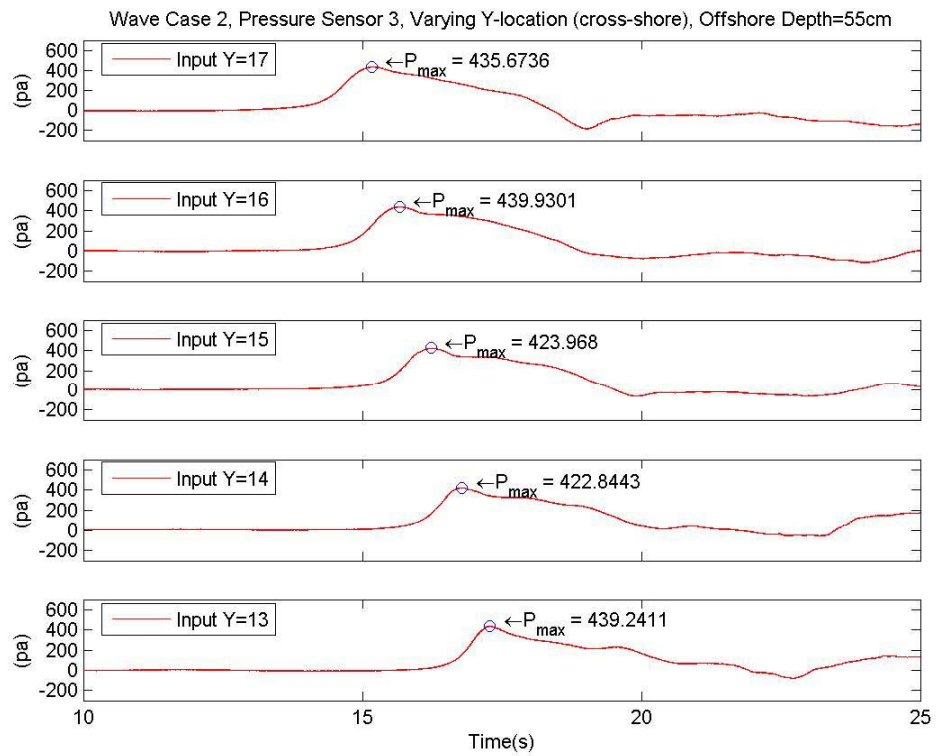


Figure 45, Pressure time Histories for increasing cross-shore distance at pressure sensor 3

### **5.3.2 Varying cylinder orientation**

To see how the pressure varies along the cylinder face, runs were performed where the test cylinder was rotated in 30 degree increments. These runs provided insight into what the pressure distribution looked like as a result of the impacting cases.

#### **5.3.3.1 Case 1**

The original coordinate system used for the pressure cylinder testing had 0 degrees normal to the wavemaker. This coordinate system was adjusted to align 0 degrees with the angle normal to the incident wave. This was necessary because the incoming waves had their direction changed by the refraction that occurred as the waves progressed over the bathymetry and into the harbor. Figure 39 demonstrates the bathymetry that leads to the entrance of the harbor. Figure 39 has four blue arrows that correspond to the original orientations of 0, 330, 300, and 270 going from left to right in the picture. It can be observed that the harbor bottom entrance is roughly perpendicular to an orientation between 270 and 0 degrees. The angle of incidence for case 1 was calculated to be 328.93 degrees and case 2 was calculated to be 322.52 degrees in the existing coordinate system, where 0 is normal to the wavemaker. Rounded up to the nearest degree, the angle of wave incidence for wave cases 1 and 2 were 329 and 323 degrees. The orientations systems were adjusted for each case with 330 degrees becoming 1 degree, and 330 for case 2 becoming 7 degrees. The orientation angles going around clockwise on the cylinder were all adjusted accordingly, and are notated with an asterisk to signify an

adjusted orientation. The method for calculating the angle of wave incidence is explained in chapter 6.

Figure 46 and 48 demonstrate what the pressure distribution for case 1 looks like as a function of time. These pressure time histories were recorded at pressure sensor 2 which is at a cylinder height of 13 cm. Each orientation is shown starting with the 1\* degree orientation, which is most normal to the incident wave. As expected, 1\* degree has the largest impact pressure of all the orientations.

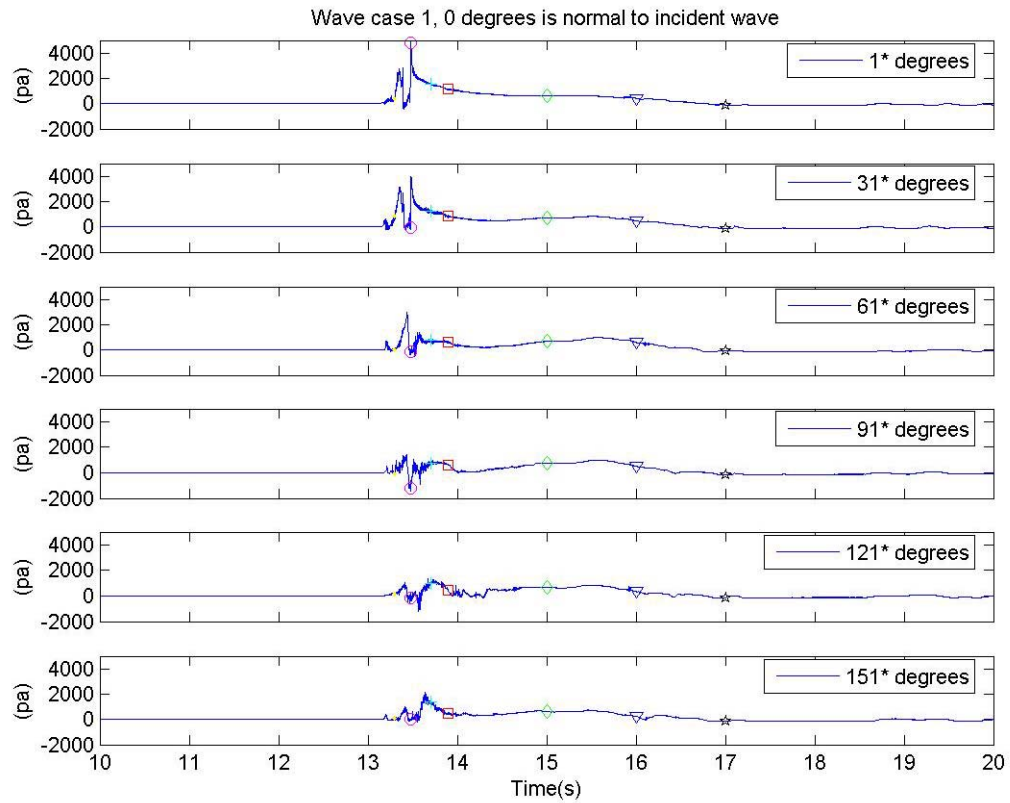


**Figure 46, Pressure Time histories for orientations 1-151 degrees, at pressure sensor 2**

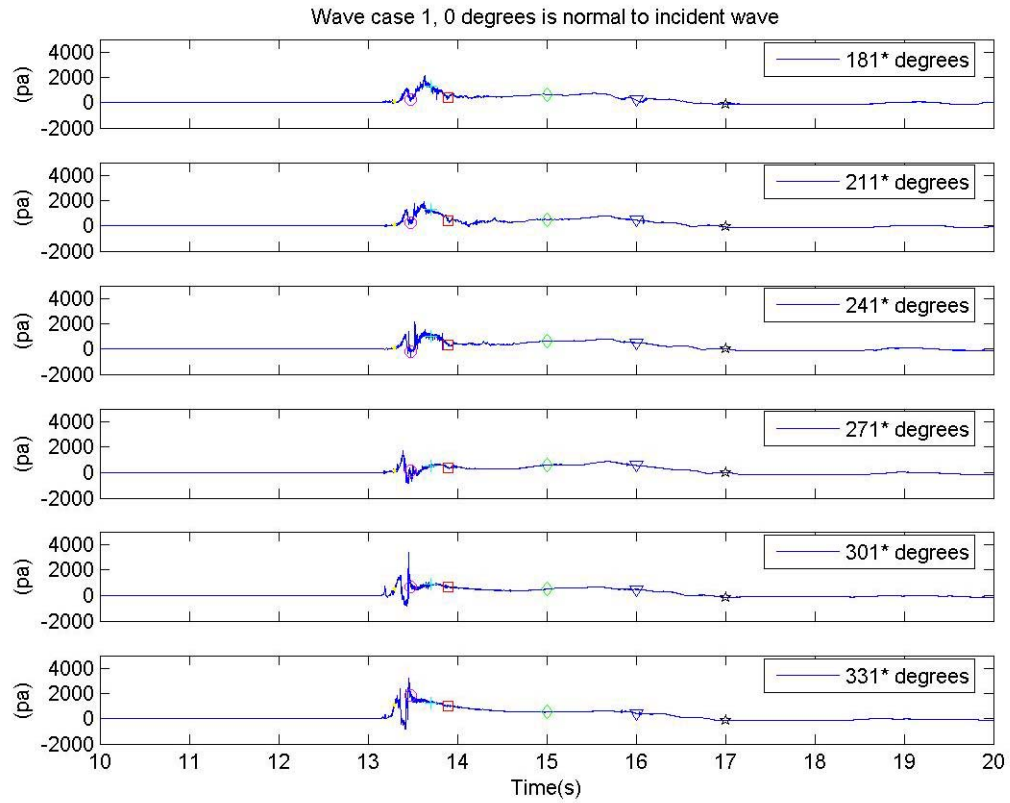


**Figure 47, Pressure time Histories for orientations 181-331 degrees, at pressure sensor 2**

In Figure 46 and 48 different color shapes can be seen along the time series. These shapes specify a specific point in time. Figure 48 shows a graph of the pressure distribution along the cylinder at different points in time. These colors and shapes used to distinguish each pressure distribution in Figure 48 coincide with the colors used for the time points in Figures 47 and 48.

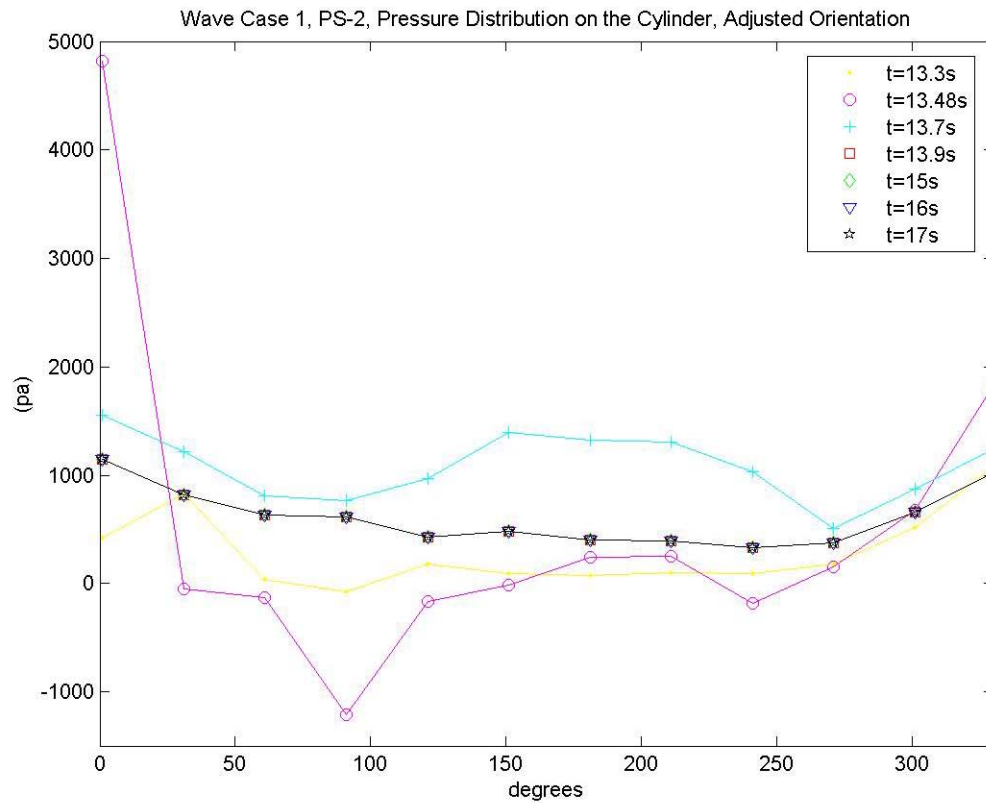


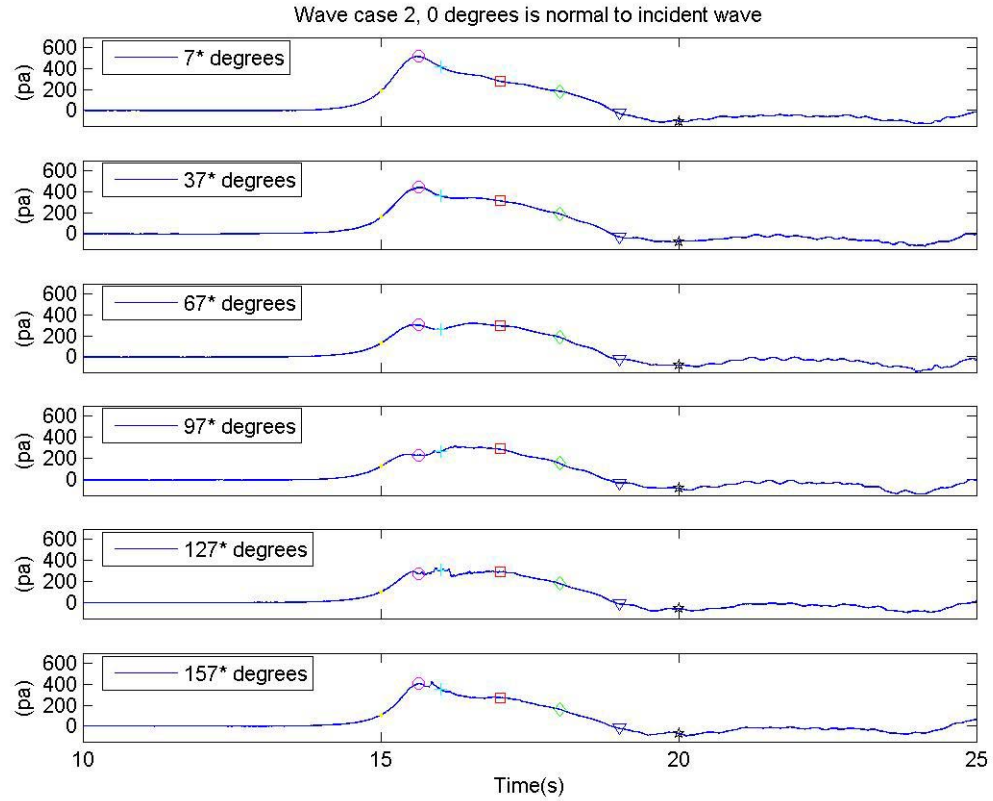
**Figure 48, Pressure distribution around the cylinder, case1**

As seen from Figure 48, the impact point of 13.48 s shows the largest variance in pressure. The pressure is highest at the cylinder face that is normal to the incident wave and then decreases to a negative value on both sides of the cylinder, while increasing back up to a positive pressure on the backside of the cylinder. All of the pressure distributions show a similar trend but have a lower variance in the pressure field around the cylinder.

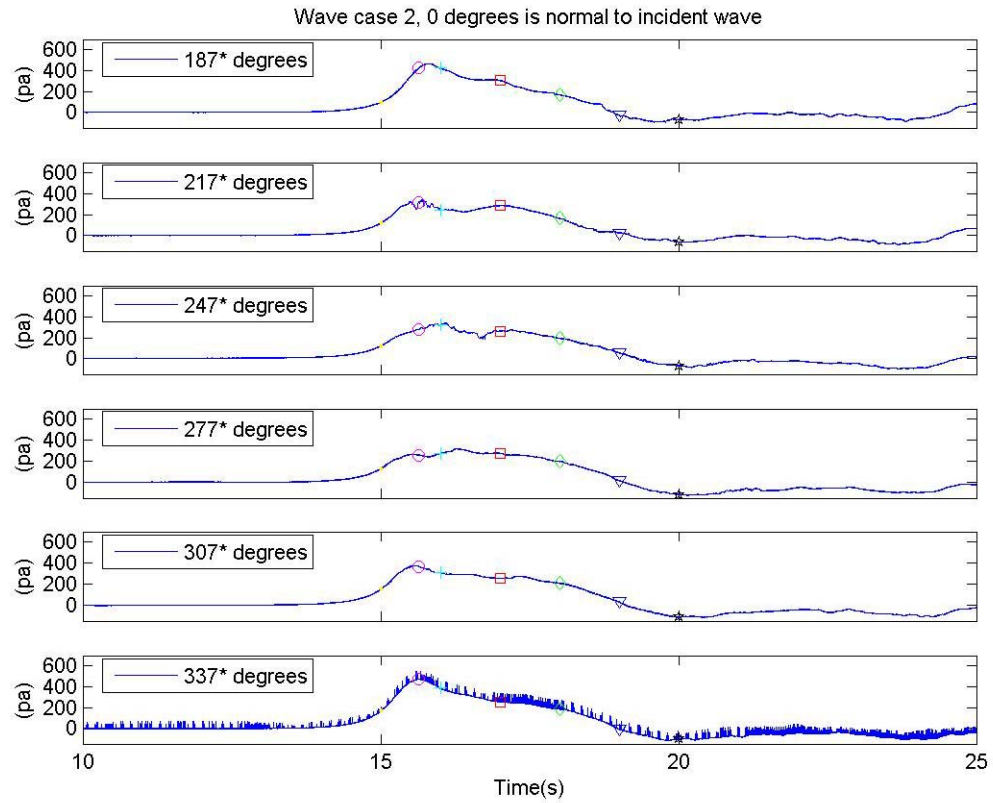
### 5.3.3.2 Case 2

Figure 49 and 51 demonstrate what the pressure distribution for case 2 looks like as a function of time. These pressure time histories were recorded at a pressure sensor which

is at a cylinder height of 13 cm. No pressure spike is seen in any of the orientation angles, due to the fact that case never breaks in the harbor. It can also be seen that the change in the profile of the pressure distribution is small when compared to that of case 1.



**Figure 49, Pressure time histories for orientations 7-157 degrees, at pressure sensor 2**



**Figure 50, Pressure time histories for orientations 187-337 degrees, at pressure sensor 2**

Figure 51 shows a graph of the pressure distribution along the cylinder at different points in time, as a result of case 2 impacting the cylinder. At the point of impact of 16.35 s, and right after impact at 16 s the pressure distribution along the cylinder roughly follows that of measured distributions of flow around a cylinder. About a second and a half after impact, the pressure distribution is seen to flatten out along the cylinder.



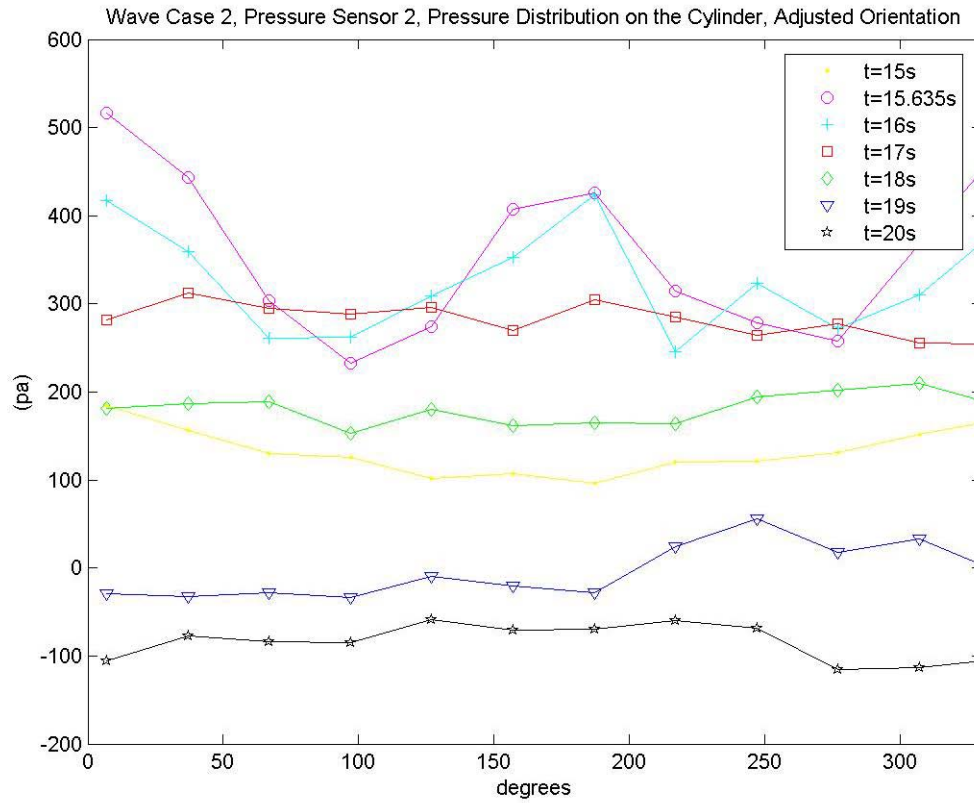


Figure 51, Pressure distribution around the cylinder, case2

### 5.3.3.3 Comparison to Reference Pressure Distribution

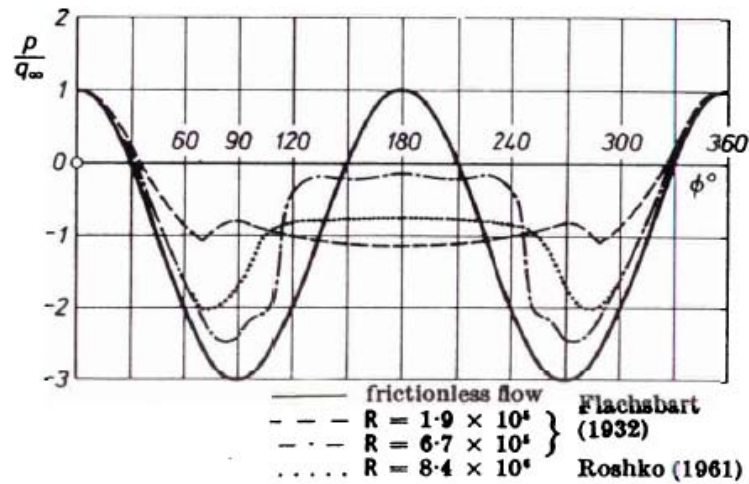


Figure 52, Pressure distribution on a cylinder, in steady flow (Schlichting, 1979)

Figure 52 is a plot of the pressure distribution on a circular cylinder in the subcritical and supercritical range of Reynolds numbers. In figure 53, the term on the vertical axis under the p is the velocity squared, multiplied by the water density, multiplied by  $\frac{1}{2}$ . This was done to normalize the pressure terms. Figure 53 also represents the pressure distribution on a circular cylinder caused by the motion of the cylinder through fluids at rest, or fluids flowing through pipes or channels around the motionless cylinder. Although figure 47 represents steady flow around a cylinder, not wave flow around a cylinder, basic comparisons can still be made of the overall trends seen in pressure distribution. Overall the pressure distributions for cases 1 and 2 most closely followed the pattern of the solid line in figure 53, which is the theoretical pressure distribution for critical flow. Case 2, which is a non-breaking wave, had a very symmetrical pressure distribution. Case 1, which is a broken wave, had a large pressure at zero degrees which is normal to the wave, but the pressure at 180 degrees on the back of the cylinder was much smaller. The Reynolds (Re) Numbers for case 1 and 2 were  $2.78 \times 10^4$  and  $4.5 \times 10^3$ . The Re numbers for cases 1 and 2 were based off of a local measured  $u$  values of 1.2 m/s and 0.28 m/s. Figure 53 shows that as the Re number increases, the pressure distribution around the cylinder should more follow the frictionless flow pattern. This is not seen with cases 1 and 2, where case 2 which has the lower Re Number more closely followed the distribution of the frictionless flow. More testing needs to be performed so a true comparison can be conducted on steady flow pressure distributions around a cylinder and wave flow pressure distributions around a cylinder.

## Chapter 6

### ANALYSIS

#### **6.1 Conversion of measured pressures to force**

##### **6.1.1 Impact force on a wedge of the cylinder**

In order to obtain the magnitude of the horizontal force on the cylinder it was necessary to integrate the pressure around the cylinder. The resultant horizontal force on the cylinder was calculated by integrating the measured pressures along the vertical cylinder face and breaking each component into cross and longshore tank components.

The first step in finding the resultant horizontal force was to find the cylinder orientation where the maximum pressure was recorded. This turned out to be the 330 degree orientation angle for the cylinder, for both cases 1 and 2. Then the time where the maximum pressures occurred at each pressure sensor 1-3 were noted. For case 2, the maximum pressure at pressure sensor 2 and 3 occurred at the same time. For case 1, the maximum pressure at sensor 1 occurred before sensors 2 and 3 were even reading a pressure difference. This time was not used, because the overall pressure on the cylinder would not be reflective of the maximum force of the incoming bore for case 1. It was decided to select the time of maximum pressure occurrence based on sensors 2 and 3, when the incoming bore wave had impacted the entire face of the cylinder. The

maximum pressures at sensors 2 and 3 occurred almost simultaneously, therefore a time was selected in-between the time of maximum pressure occurrence at sensors 2 and 3. From this selected time, the pressures at each sensor, for each orientation were recorded. The assumption was made, that the pressure readings made at a given orientation were reflective of the pressures on the cylinder going 15 degrees to each orientation. For example, the pressures recorded at 30 degrees, were assumed valid for the orientations of 15 through 45 degrees on the cylinder face.

Next, the pressures recorded at each sensor were used to make a slope of pressure to cylinder height. For case 2, since only 2 pressure sensors, 2 and 3, were impacted by the wave, a slope of the pressure/cylinder height was calculated. Although not drawn to exact scale, figure 53 diagrams where the pressure sensors were in regards to the incoming wave, and the still water level. Also shown in figure 53, is a sketch of the predicted pressure distribution that will be seen on the vertical face of the cylinder, at the orientation that is most normal to the incoming wave. As seen in figure 53, the still water level of 13.5 cm in the harbor, was just a little above pressure sensor 2 which was located 13 cm up on the cylinder face. Pressure sensor 1 located at 26 cm was well above the incoming wave caused by case 2, which had a maximum height of 18 cm at this location.

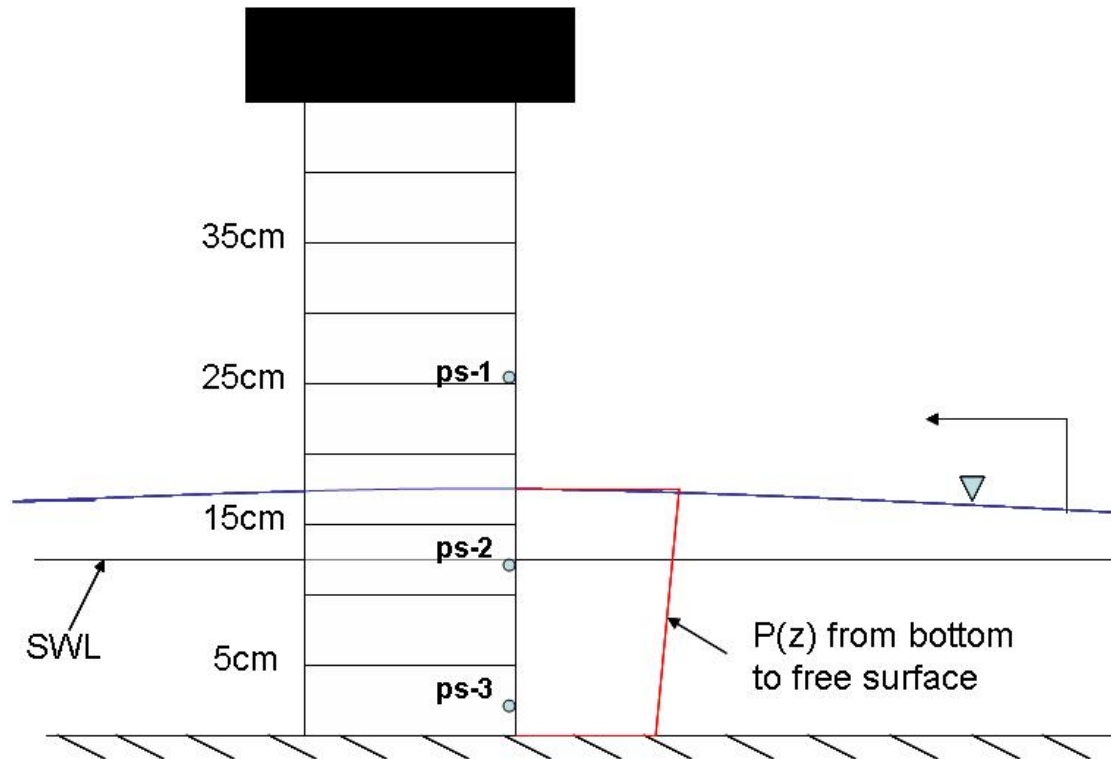


**Figure 53, Diagram of case 2 impacting the cylinder**

The assumption was made that the impacting pressure on the cylinder face would have a linear relationship with height on the cylinder. For case 2, the pressures at the bottom of the cylinder and at the water surface were calculated using this slope. The height used for the water surface was from the measured water surface elevation, found from using wave gauges. Figure 54 shows the 2 measured pressures for pressure sensor 2 and 3 that form the pink line, and the dark blue and yellow lines signify the slope of the pink line extracted out to the bottom of the harbor floor, and up to the water surface at 0.18 m. Since pressure measurements were not taken above the SWL, or near the free surface, it was decided that the most conservative estimate for the pressure at the free surface would be from the same linear slope found from sensors 2 and 3 applied all the way to the free surface.

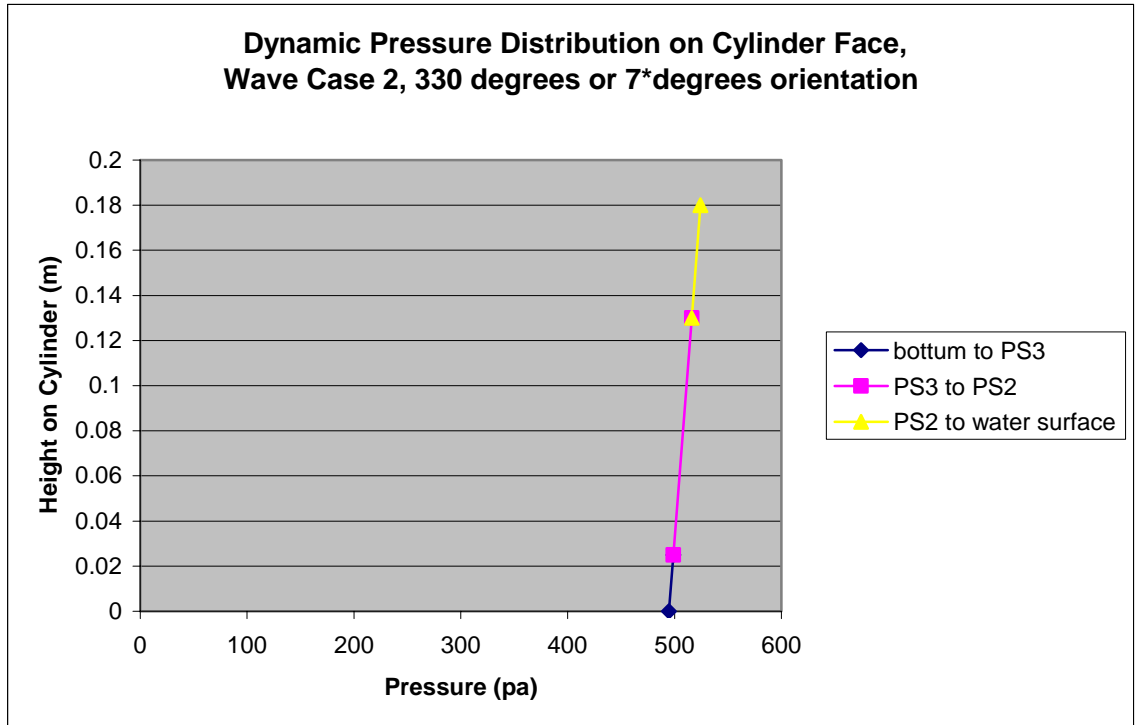


**Figure 54, Plot of pressures along the vertical cylinder face for case 2**

Case 1 was similar, but pressures were recorded at three sensors due to the larger wave condition. As seen in figure 55 pressure sensor 2 was located at the still water level, and pressure sensor 1 was located 0.6 mm below the peak of the incoming bore. It was assumed that the pressure recorded at pressure sensor 1 was reflective of the pressure at the free surface. Figure 55 also shows an approximation of the pressure distribution along the vertical face most normal to the incoming wave.

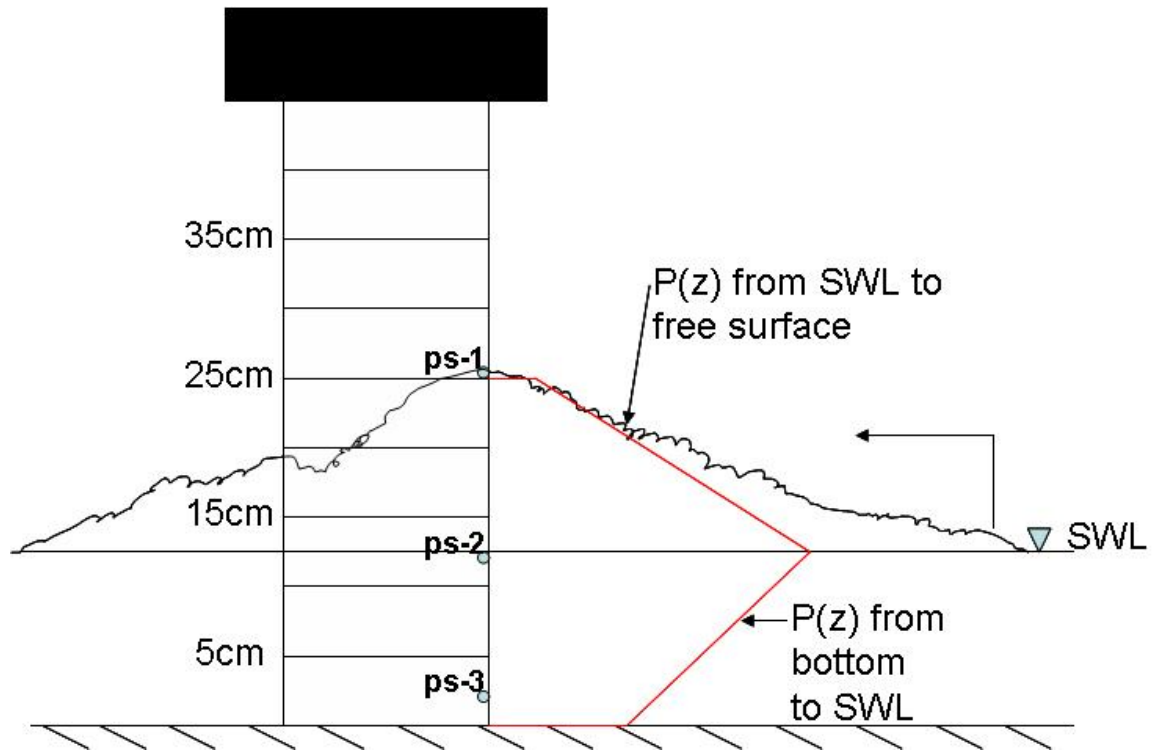


**Figure 55, Diagram of case 1 impacting the cylinder**

Therefore two slopes were calculated, one for the change in pressure from pressure sensor 1 to the pressure sensor 2, and a second from pressure sensor 2 to pressure sensor 3. The slope from pressure sensor 2 to 3 was assumed to be constant to the bottom, and therefore was used to predict the pressure at the bottom of the cylinder. As in case 2, it was assumed that the vertical pressure distribution was linear in between measured points. Figure 56 shows the 2 measured slopes in the yellow and pink lines. The dark blue line represents the SWL to pressure sensor 3 slope carried out to the harbor floor.

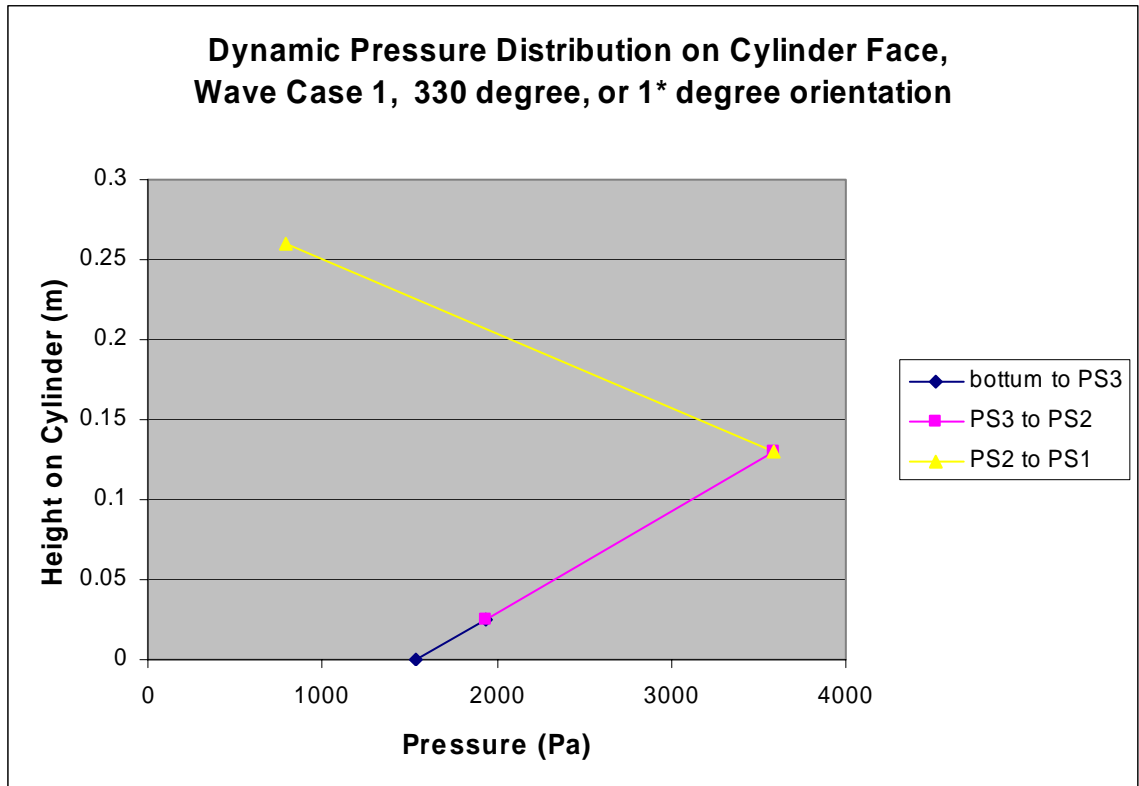


**Figure 56, Plot of pressures along cylinder face for case 1**

This change in slope that occurs above the still water line is also seen in tests where pressures were measured along the vertical faces of rectangular breakwaters. Figure 57 is from Goda (2000). Figure 57 shows the vertical pressure distribution of wave pressure on a caisson breakwater. For Goda wave pressure formulas he assumes trapezoidal pressure distributions along the vertical faces of breakwaters, regardless of whether the waves are breaking, nonbreaking, or broken. Qualitative comparisons can be seen from the measured vertical pressure distributions as seen in figures 54 and 56, and the theoretical pressure distribution predicted by Goda in figure 57.



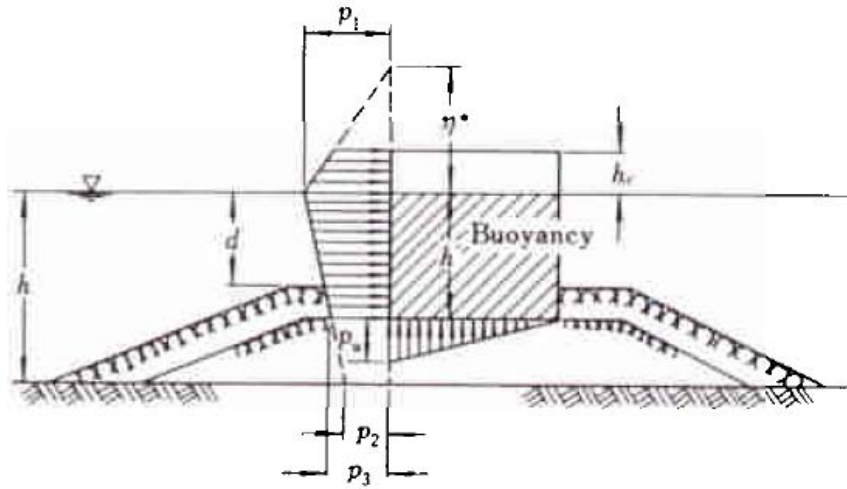


**Figure 57, Distribution of wave pressure on an upright section of a vertical breakwater.**

With the pressure distributions known for each orientation, it was now possible to integrate the pressure distribution over the height of the impacting wave. The trapezoid rule was used to integrate the pressure, and solve for the resultant force on each wedge. Equation 6.1 was used to calculate the force on the cylinder wedge for case 1.

$$F = w(h_2) \frac{(p_2 + p_b)}{2} + w(h_{ws} - h_2) \frac{(p_{ws} + p_2)}{2} \quad (6.1)$$

The variables  $h_2$  and  $h_{ws}$  are the heights of pressure sensor 2, and the water surface. The variables  $p_2$ ,  $p_3$ ,  $p_b$ , and  $p_{ws}$  are the pressures at sensors 2, 3, the harbor bottom, and the water surface. The  $w$  variable is the width of 1/12 of the circumference, being that 12 cylinder orientations were measured. The areas of two trapezoids are calculated, being that the pressure distribution for case 1 was split into two trapezoid shapes as seen in figure 57. Equation 6.2 was used to calculate the force on the cylinder wedge for case 2.

$$F = w(h_{ws}) \frac{(p_{ws} + p_b)}{2} \quad (6.2)$$

For case 2, only the area for one trapezoid was calculated being that the pressure distribution was one trapezoid ranging from the harbor bottom up to the water surface of the wave, as seen from figure 54. Figure 58 and 59 show the force delivered by cases 1 and 2 on the orientation wedges. It can be seen that for both cases, the maximum force occurs at the cylinder orientation most normal to the incident wave. The max wedge forces of 25 N and 3.7 N for cases 1 and 2, correspond to 5.62 lbf and .83 lbf. These magnitudes seem reasonable for the waves that produced them. The orientation angle where the maximum force occurs is the 330 degree wedge in the original coordinate system. This corresponds to 1 degree for case 1 and 7 degree for case 2 in the adjusted orientation systems.

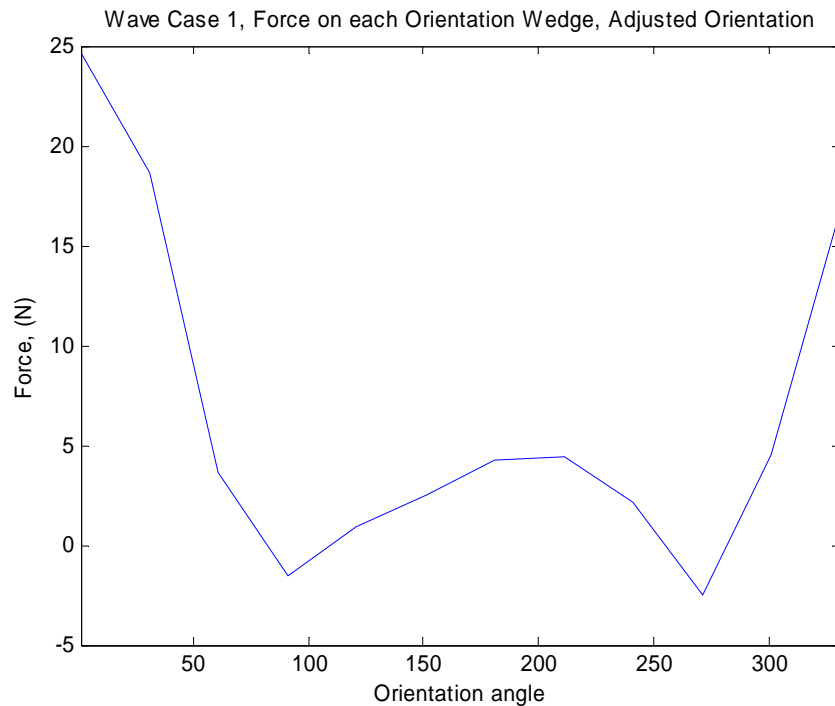


**Figure 58, Force on each wedge orientation, case 1**



**Figure 59, Force on each wedge orientation, case 2**

### **6.1.2 Resultant impact force on the cylinder**

In order to determine the resultant force from all the different orientations, each wedge force was broken into its longtank and crosstank components. All of the longtank components for each wedge force were summed up, with the crosstank wedge force components also being summed up. These two summed force components were squared, added up, and then the square root was taken. This method utilizing the Pythagorean Theorem provided the resultant force acting on the cylinder. As seen in Figure 60, the angle of wave incidence that produced the resultant force could also be calculated as a result of the summed up long and crosstank force components.

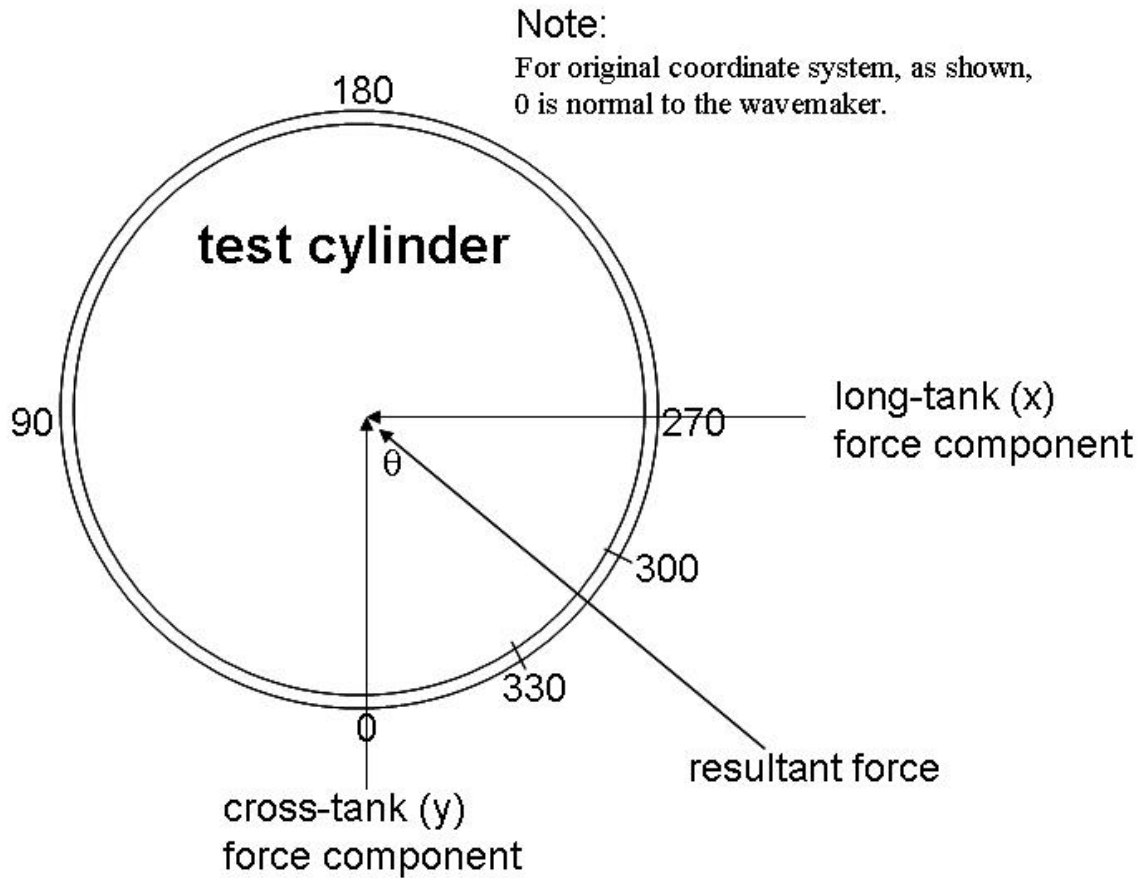


**Figure 60, Diagram of long and crosstank force components, and resultant force**

The resultant impact force for case 1 was 24.60 N, and the resultant force for case 2 was 2.11 N. This resultant force is important for design, in that this force will determine what the potential overturn moment is for the maximum incoming waves. This resultant force will also determine the shear force being applied at the base of the cylinder, or pier by the maximum incoming waves.

### **6.1.3 Resultant direction of the impact force**

Utilizing basic trigonometry, the wave incident angles were calculated by taking the arctangent of the longtank summed force divided by the crosstank summed force. This provided the angle theta ( $\theta$ ) as seen from figure 60. This angle theta was added to 360

degrees to find the angle in the adjusted coordinate system. The resultant angle of wave incidence was 329 degrees for case 1, and 323 degrees for case 2.

## 6.2 Determining the period (T) of cases 1 and 2

### 6.2.1 Period from estimated method

Two methods were used to obtain the period of cases 1, and 2. The first method was simply to see look at the water surface time history of each case at its most offshore point. Figure 61 is a plot that focuses on the initial wave produced by case 2 as it passes by the wave gauges. The blue line marks the average wave height of the wave gauges, and the red line signifies the still water line. The time at both intersections of the blue and red lines can be used to approximate what half of the effective period is. From figure 61 the effective periods for case 2 can be approximated to be 9 seconds.

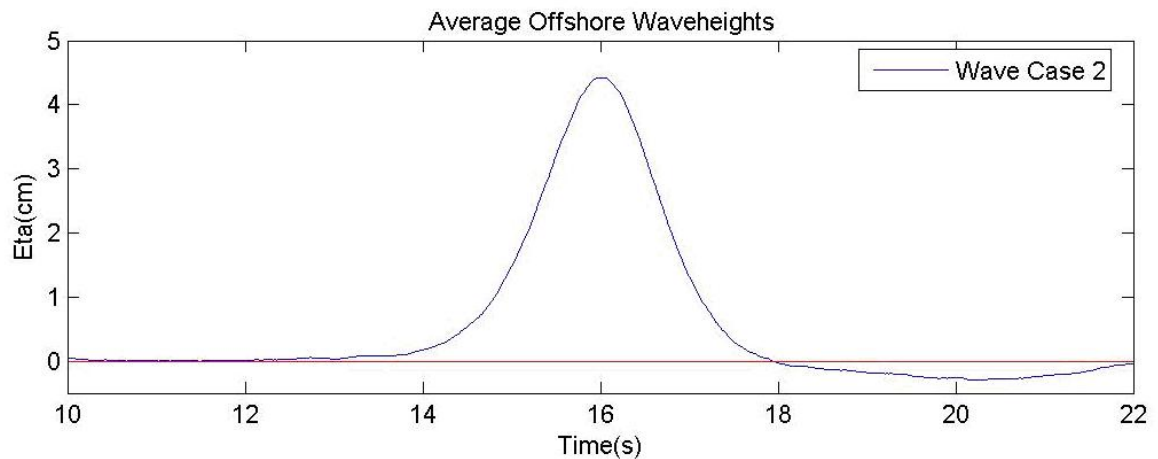


Figure 61, Plots of cases 1 and 2

### 6.2.2 Period from theoretical method

In order to calculate the period of cases 2, it was necessary to calculate the wavelength ( $L$ ) of each case. Using a method developed for solitary waves, a measure of the

wavelength can be defined in terms of wave height ( $H$ ) and water depth ( $d$ ). Equation 6.3 shows the equation used to calculate the wavelength.

$$L = \frac{2d}{\sqrt{.75H}} \operatorname{arc} \cosh \sqrt{\frac{1}{.05}} \quad (6.3)$$

In equation 5 the wavelength is equal to the distance between two points in the symmetric surface profile (one near the front and one near the tail) where the height is 0.05 of the height at the crest  $H$ . (Synolakis, 1987) The wavelength for case 2 using equation 6.3 worked out to 13.14 m.

Next using equation 6.4 for the velocity and surface profile of a progressive wave, the period could be solved for.

$$u = \frac{H}{2} \frac{gk}{\sigma} \frac{\cosh k(d+z)}{\cosh(kd)} \cos(kx - \sigma t) \quad (6.4)$$

Equation 6.4 has the horizontal water particle velocity on the left represented by the variable  $u$ . The variable  $k$  is the wave number, and is equal to  $2\pi/L$ . The variable  $\sigma$  is the angular frequency, and is equal to  $2\pi/T$ . The variable  $h$  represents the water depth offshore, which would be 55 cm for case 2. The variable  $z$  represents the distance from the still water line to the water surface. In this equation the last term goes to 1, in that the horizontal position ( $x$ ) and the time ( $t$ ) can both be assumed to be 0. The period for case 2 was 12.07 s after rearranging and solving for  $T$ . These  $T$  values found from both methods can be seen in table 4.

**Table 4, Period values for waves cases 1 and 2, using measured and theoretical methods**

Case	T, Method 1	T, Method 2
-	(s)	(s)
2	9	12.07s

## 6.3 Morison equation approximation for case 2

### 6.3.1 Results from the Morison equation applied to case 2

Table 5, Guide for evaluating wave load calculation procedures (Randal, 01)

K	D/L < 0.2	D/L > 0.2
K > 25	Drag dominated. Morrison equation with $C_m$ and $C_d$ . $Re > 1.5 \times 10^6$ ; $C_m = 1.8$ , $C_d = 0.62$ $10^5 < Re < 1.5 \times 10^6$ ; $C_m = 1.8$ , $C_d$ varies from 1.0 to 0.6	Morrison equation should not be used for computing wave forces. Diffraction theory used.
5 < K < 25	Drag and inertia dominated range Morrison equation applicable, but $C_m$ and $C_d$ values show large scatter. Flow behavior and load are complex and uncertain. $Re > 1.5 \times 10^6$ ; $C_m = 1.8$ , $C_d = 0.62$ .	
K < 5	Inertia dominated range. Morrison equation or Diffraction theory is used. $C_m = 2.0$ Effect of drag is negligible	

Definitions: Keulegan-Carpenter Number,  $K = U_m T/D$ ; Reynolds Number,  $Re = U_m D/\nu$ ;  $C_m$  = inertia coefficient;  $C_d$  = drag coefficient;  $U_m$  = peak velocity;  $T$  = wave period;  $\nu$  = kinematic viscosity; and  $D$  = diameter.

Table 5 shows the method used for selecting which equation to use in solving for the maximum force from an unbroken wave. From this table it can be observed that the ratio of diameter over wavelength ( $\frac{D}{L}$ ) is used to classify which force calculation procedure should be used. It can also be seen from table 5 that the magnitude of Keulegan-Carpenter (Ke) and Reynolds (Re) play an integral part in selecting which coefficients of drag and inertia to use. The equations for both the Re and Ke numbers can be found in equations 6.5 and 6.6.

$$Re = \frac{U_m D}{\nu} \quad (6.5)$$

$$Ke = \frac{U_m T}{D} \quad (6.6)$$

The Re number is calculated by multiplying the peak water particle velocity ( $U_m$ ) and the diameter ( $D$ ) divided by the kinematic viscosity ( $\nu$ ). The Ke number is calculated by

multiplying the  $U_m$  and  $T$  divided by the  $D$ . Table 6 shows the estimated and theoretical periods found for case 2 and the Ke numbers produced from each method of determining  $T$ .

**Table 6, Case 2, values from measured and theoretical periods (T)**

Method of obtaining T	T	D/L	Ke	Re	Cd	Cm
-	(s)	-	-	-	-	-
Estimated (1)	9	0.019	2.14	27800	1.46	1
Theoretical (2)	12.07	0.012	6.39	27800	1.47	1.13

The  $C_m$  and  $C_d$  values specified in table 5 are correct, but more accurate coefficients can be found from empirically derived graphs. Graphs that have  $C_m$  and  $C_d$  as a function of the Re and Ke numbers were used to locate the most accurate values for  $C_m$  and  $C_d$ . The  $C_m$  and  $C_d$  values found are shown in table 6.

Although the periods found from the estimated and theoretical methods were quite different, the values of  $C_d$  and  $C_m$  remained similar as seen in table 6. Therefore the drag, inertial, and total forces produced were very similar in magnitude.

Table 7 is a comparison of the measured and Morison equation derived maximum force delivered by case 2 on the test cylinder. It shows that the maximum force obtained from integrating the measured pressures around the cylinder is considerably lower in magnitude than the maximum force obtained from the Morison equation. The maximum Morison force values seen in table 7 were calculated by multiplying the maximum total force per unit length values by the sum of the water depth in the harbor and the wave height at the cylinder. This length for case 2 was 18 cm.



Table 7, Comparison of maximum force on the cylinder, case 2						
measured force		force from Morison equation				
from pressure sensors	force from estimated T	actual error	percent error	force from theoretical T	actual error	percent error
(N)	(N)	(N)	%	(N)	(N)	%
2.11	11.47	-9.36	443	11.56	-9.45	448

### 6.3 Cross approximation for case 1

The Cross equation, shown in equation 2.3, is an approximation to estimate the impact force on a wall from a progressing surge. The force coefficient ( $C_f$ ) in this equation is dependent on the wedge angle ( $\theta$ ) of the bore. This wedge angle is explained in chapter 2, and shown in figure 1. As the wedge angle increases the force coefficient increases asymptotically, as seen in figure 64.

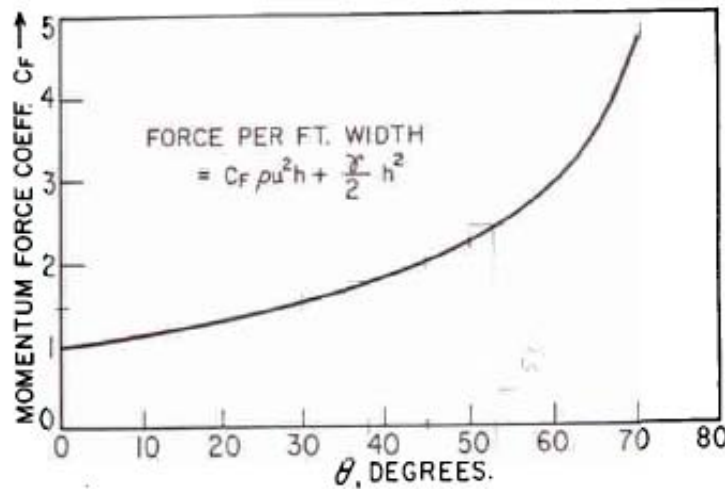
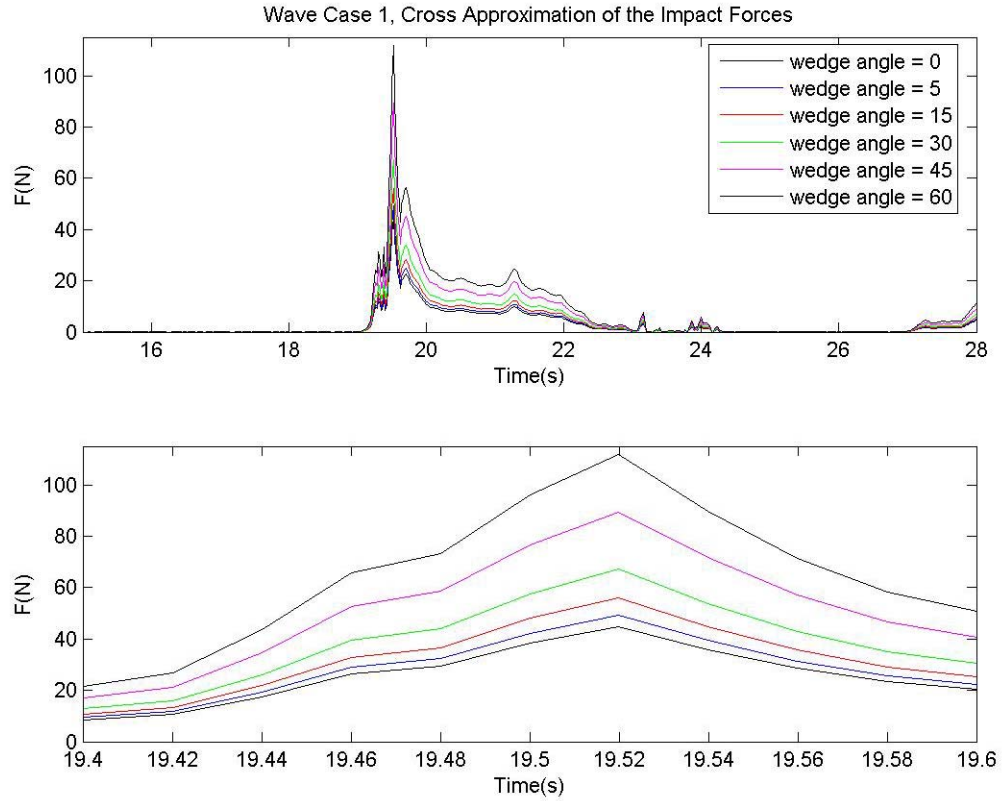


Figure 62, Plot of  $C_f$  versus  $\theta$

In order to make this equation suitable for the force on a cylinder instead of rectangular wall, the width term  $b$  had to be changed from the rectangular width of the wall to half of the circumference of the cylinder. Using a range of values for wedge angle, the

maximum force on the cylinder was calculated using the Cross method. Figure 63 shows what the maximum force looks like for varying wedge angles.



**Figure 63, Cross method for case 1**

The maximum force found from integrating the measured pressures around the cylinder for case 1 was 47.69 N. This value of roughly 50 N would correspond to a wedge angle in the range of 5 to 15 degrees, as seen from the bottom plot in figure 65. From visual observations of the bore created by case 2, no pictures were available, the wedge angle appeared to be a shallow angle, and in the range predicted by the Cross method.

## Chapter 7

### CONCLUSION

#### **7.1 Estimation of broken wave force**

Although the Cross equation was derived to calculate the maximum force of a surge hitting a rectangular wall, once it was converted to the force on a cylinder it did quite well. In order to get a true assessment of how well the Cross equation performed, it would be necessary to have video and fast action still pictures taken of the wave as it entered the harbor and went over the location where the test cylinder was.

#### **7.2 Estimation of unbroken wave force**

The Morison equation produced a maximum impact force that was much larger than the maximum impact force found from converting the measured pressures to a force. Both the estimated and theoretical periods found for case 2 produced similar coefficients of drag and inertia. This meant that the total force from the Morison equation was nearly identical from both methods of determining the wave period. Overall it is hard to determine why the measured and Morison produced forces are so different. It is generally understood that the Morison equation is a conservative method for determining

the maximum impact force of an unbroken wave, but that alone does not explain the large discrepancy in the results.

### **7.3 Future works and recommendations**

In order to better validate both the Morison equation and the Cross equation, for unbroken and broken waves the following things should be done. More pressure sensors, if available, should be vertically flush mounted to the cylinder face, so that a more accurate approximation of the pressure distribution can be made. A smaller cylinder rotation of 5 degrees as opposed to 30 degrees would also help to provide a more accurate pressure distribution around the test cylinder. Lastly, as mentioned above, video and photographs should be taken from the side view of the incoming wave so that a reasonably good estimate can be made of the bore wedge angle.

## BIBLIOGRAPHY

Acosta, J. A., Hauptmann E. G. and Sabersky, R.H. (1989). *Fluid Flow, a First Course in Fluid Mechanics*, third Edition, Macmillan Publishing Company, New York.

Amason, Halldor. (2005). *Interactions between an Incident Bore and a Free-Standing Coastal Structure*, dissertation for degree of Doctor of Philosophy, University of Washington.

Briggs, M. J., Harkins, G. S., Hughes, S. T. and Synolakis, C. E. (1995) large Scale Three-Dimensional Laboratory Measurements of Tsunami Inundation, *Tsunami: Progress in Prediction, Disaster Prevention and Warning*, 129-149.

Cross, R. H. (1967). Tsunami Surge Forces, *Journal of Waterways and Harbors Division*, ASCE 93(4): 201-203.

Cumberpatch, E. (1960). The impact of a water wedge on a wall, *Journal of Fluid Mechanics* 7:353-374.

Dalrymple, R. A., and Dean, R. G. (1991). *Water Wave Mechanics for Engineers and Scientists*, World Scientific, New Jersey.

Department of the Army-U.S. Army Corps of Engineers. (1984) Shore Protection Manual Volume II, U.S. Government Printing Office.

Fox, R. W., Pritchard, P.J. and McDonald, A. T. (2004). *Introduction to Fluid Mechanics*, sixth edition, John Wiley & Sons Incorporated, New Jersey.

Goda, Y. (2000). *Random Seas and Design of Maritime Structures*, World Scientific, New Jersey.

Hajime, M., Hamzah, M. A. and Takayama, T. (2000). Simulation and Experiment of Hydrodynamic Pressure on a Tsunami Barrier, *Coastal Engineering*: 1501-1507.

Hughes, S. A. (1993). *Physical Models and Laboratory Techniques in Coastal Engineering*, World Scientific, New Jersey.

“Indian Ocean Earthquake.” Wikipedia, the free encyclopedia. 2004. 6 Oct. 2005 <[http://en.wikipedia.org/wiki/2004\\_Indian.Ocean\\_earthquake](http://en.wikipedia.org/wiki/2004_Indian.Ocean_earthquake)>.

Liu, P. F., Synolakis, C. and Yeh, H. H. (1991) Report on the International Workshop on Long Wave Run-up, *Journal of Fluid Mechanics* 229: 675-688.

Madsen, P. A. and Svendsen, I. A. (1983). Turbulent bores and hydraulic jumps, *Journal of Fluid Mechanics* 129: 1-25.

Oumeraci, H and Wienke, J. (2005). Breaking wave impact force on a vertical and inclined slender pile-theoretical and large-scale model investigations, *Coastal Engineering* 52: 435-462.

Peregrine, D. H. and Svendsen, I. A. (1978). Breakers, Bores, Jumps, *Coastal Engineering* (30): 540-548.

Randall, R. E. (1997). Elements of Ocean Engineering, The Society of Naval Architects and Marine Engineers, New Jersey.

Schlichting, Herman. (1987). *Boundary-Layer Theory*, McGraw\_Hill Book Company, New York.

“Tsunami.” Wikipedia, the free encyclopedia. 2004. 6 Oct. 2005  
<<http://en.wikipedia.org/wiki/Tsunami>>.

# APPENDIX

## Appendix 1



**Figure 64, Group Photo of Project Team**

Figure 60 is a photo that shows all the people that participated in the “Tsunami-Inundation” project. The people from left to right are James (Jim) Lynch, Daniel Grant, Shingo Ichikawa, Charlie Bisgard, Christopher (Cris) Johnson, and Yusuke Matsumura. Jim Lynch was in the Research Engineering Undergraduate (REU) program, and is currently a senior at University of Wisconsin at Platteville. Daniel Grant was part of the wave laboratory staff, and he is currently a senior at Corvallis Highschool. Shingo Ichikawa is a student in the OSU ocean engineering program, and will graduate after the Fall 2005 term. Cris Johnson was also part of the wave laboratory staff, and he is

currently a senior in the OSU civil engineering program. Yusuke was on a month long exchange program from Japan. He is currently a junior at the University of Tokyo.